A conservative interface method for compressible flows

X Y Hu [a] B C Khoo [b] N A Adams [a] F L Huang [c]

[a]*Lehrstuhl für Aerodynamik, Technische Universität München*
85747 Garching, Germany

[b]*Department of Mechanical Engineering, National University of Singapore*
117576 Singapore, Singapore

[c]*National Key Laboratory for Prevention and Control of Explosive Disasters,*
Beijing Institute of Technology
100080 Beijing, China

Abstract

In this work, we present a conservative interface method for both multi-fluid and complex boundary problems, in which the standard finite volume scheme on Cartesian grids is modified by considering computational cells being cut by interface. While the discretized governing equations are updated conservatively, the method treats the topological changes naturally by combining interface description and geometric operations with a level set technique. Extensive tests in 1D are carried out, and 2D examples suggest that the present scheme is able to handle multi-fluid and complex (static or moving) boundary problems in a straight-forward way with good robustness and accuracy.

Key words: compressible flow, multi-fluid problem, complex boundary, level set function

1 Introduction

Various numerical methods have been developed to simulate and study the dynamics of compressible flows at high speeds. In all cases, a significant difficulty encountered with these numerical computations is the treatment of a material interface. In general, there are two main types of interface related problems: one is the multi-fluid problem in which the interface separates interacting different fluids; the other is the complex boundary problem in which the interface defines a complex, static or moving, boundary between the fluid and a rigid solid wall or a body.

Manuscript of Xiangyu Hu   *5 April 2006*

Usually, the interfaces for these two types of problems are treated in quite different ways. For a multi-fluid problem, the interface is often defined on a Cartesian grid as a transition region with a steep gradient. Some numerical methods using this 'smeared' interface representation are the volume of fluid (VOF) method (Hirt and Nichols 1981; Young 1982; Abgrall and Karni 2001) or constrained interpolation profile (CIP) method (Yabe et al. 2001). For a complex boundary problem, the interface is often defined as a non-smeared boundary of a structured body-fitted grid (Benek et al. 1987), or an unstructured grid (Jameson et al. 1986; Peraire et al. 1987; Löhner, 1987). On the other hand, there are still alternative approaches in which the above two types of interfaces are both treated on a Cartesian grid. One approach is to reconstruct a "smeared" complex boundary with the VOF technique (Hirt 1993). The other approach is to track both multi-fluid interfaces and complex boundaries with a non-smearing representation. Glimm et al. (1981) track the multi-fluid interface as a non-smeared internal moving boundary with a grid intersection technique. Similar geometric treatments of the boundary are also developed for Cartesian approaches to complex boundary problems (Berger and LeVque 1989; Chiang et al. 1992; Quirk 1994; Yang et al. 1997a, 1997b). Even though these mentioned alternative approaches are conceptually simple there are two major limitations: one is that defining and tracking of the interface require rather complicated procedures with the grid intersection technique, especially in the cases of large topology variations; the other is the lack of conservative properties, which usually leads to low accuracy near the interface, especially when strong or long time scale interface interactions are involved.

The level set technique (Osher and Sethian, 1988; Davis, 1992; Sussman et al. 1998) is a reasonably easy way to define and track a non-smeared multi-fluid interface. To deal with the issue of conservation, the original works of Berger and LeVque (1989) and Quirk (1994) on complex boundary problems do not treat the interface specifically but use a complex adaptive mesh refinement strategy to increase accuracy near the boundary. Other approaches, e.g. GFM (ghost fluid method) and related methods (Fedkiw et al, 1999; Chung 2001; Liu et al 2003; Hu and Khoo 2004) employ special internal boundary conditions at the multi-fluid interface in the attempt to correct or reduced conservation errors. Fairly similar procedures can also be implemented for complex boundary problems (Forrer and Jeltsch 1998; Forrer and Berger 1998; Arienti et al. 2003; Hu et al. 2005). While these approaches have led to promising results they possess strictly only a first-order convergence rate for the conservation errors. To handle the stability difficulty of a conservative discretization with the VOF method, Colella (1990) and Miller and Colella (2002) introduced a redistribution approach for multi-fluid problems in which conservation defects resulting from non-conservative updates are redistributed onto neighboring cells according to mass weighting. Falcovitz et al. (1997) satisfy conservation near a complex moving boundary by a Strang-type operator splitting. Glimm

et al. (2003) introduced a conservative method based on a grid intersection technique, in which each small-size cut cell is merged with one of its neighboring cells, for multi-fluid flows with the assumption of no topological change in the solution.

In this paper, we propose a Cartesian interface method suitable for both multi-fluid and complex boundary problems. We use a standard finite volume scheme for the far interface region which is slightly modified for the near interface region. Unlike Miller and Colella (2002), the present method updates the discretized governing equations fully conservative for both fluids individually and for interface exchanges in multi-fluid problems. Small cut cells are treated with a mixing procedure which, however, is different from the approaches found in Miller and Colella (2002) and Glimm et al. (2003). As our mixing procedure is separated from the flux updating of conservative variables, it is easy to implement, especially when complex geometries are considered. Also, unlike the work of Falcovitz et al (1997) the present method offers a fairly simple implementation in multi-dimension and multi-level time integrations without space-time splitting. The assumption of non-topological change as in Glimm et al (2003) is not necessary in our formulation. Furthermore, as the level set technique is used for the interface description and geometric operations, the method maintains the simplicity of GFM-like methods. Indeed, in our implementation, we use the interface interaction method (Hu and Khoo 2004) to obtain the interface conditions for the near interface grid points. However, these interface interactions are not employed for defining the ghost node states but for the direct calculation of momentum and energy exchanges across the interface. Accordingly, the ghost node is filled only for the stencil interpolation rather than for implementing the internal boundary condition common for GFM-like methods.

2 Overview of the method

Assuming the fluid is inviscid and compressible the governing equation of the flow can be written as a system of conservation laws

$$\frac{\partial \mathbf{U}}{\partial t} + \nabla \cdot \mathbf{F} = 0 \quad \text{on } \Omega, \tag{1}$$

where $\mathbf{U}$ is the density of the conserved quantities of mass, momentum and total energy, and $\mathbf{F}$ represents the corresponding flux functions. When an interface $\Gamma(t)$ separates the domain Ω into two sub-domains $\Omega^1(t)$ and $\Omega^2(t)$, as for a multi-fluid problem, the evolution of the interface is determined by

the interface condition defined by a two-material Riemann problem

$$\mathcal{R}(\mathbf{U}_{fluid1}, \mathbf{U}_{fluid2}) = 0 \quad \text{on } \Gamma(t). \tag{2}$$

When a complex boundary problem is considered, the evolution of the interface is determined by the boundary velocity $\mathbf{v}_{rg}$. The pressure on the interface is then determined by the one-sided Riemann problem

$$\mathcal{R}(\mathbf{U}_{fluid}, \mathbf{v}_{rg}) = 0 \quad \text{on } \Gamma(t). \tag{3}$$

The boundary velocity can be prescribed. If the associated rigid solid body moves according to an inertial coupling the acceleration $\mathbf{a}_{rg}(t)$ can be calculated by

$$\mathbf{a}_{rg}(t) = \frac{1}{m_{rg}} \int_{\Gamma(t)} p d\mathbf{s} \tag{4}$$

in which the integration is carried out over the entire interface, and m_{rg} is the solid body mass.

Following Miller and Colella (2002), we consider Eq. (1) for the fluid occupying the sub-domain Ω^1 on a two-dimensional Cartesian grid with grid spacings Δx and Δy. A finite volume discretization can be obtained from integrating Eq. (1) over the space-time volume $\Delta_{ij} \bigcap \Omega^1(t)$ of a computational cell (i, j) occupied by the fluid

$$\int_n^{n+1} dt \int_{\Delta_{ij} \bigcap \Omega^1(t)} dx dy \left(\frac{\partial \mathbf{U}}{\partial t} + \nabla \cdot \mathbf{F} \right) = 0 \tag{5}$$

where $\Delta_{ij} = \Delta x \Delta y$ is the cell volume. $\Delta_{ij} \bigcap \Omega^1(t)$ can be represented by $\alpha_{i,j}(t) \Delta x \Delta y$ where $\alpha_{i,j}(t)$ is the time dependent volume fraction of the considered fluid and satisfying $1 \geq \alpha \geq 0$. By an application of Gauss's theorem, one obtains

$$\int_n^{n+1} dt \int_{\Delta_{ij} \bigcap \Omega^1(t)} dx dy \frac{\partial \mathbf{U}}{\partial t} + \int_n^{n+1} dt \int_{\partial \Delta_{ij} \bigcap \Gamma(t)} dx dy \mathbf{F} \cdot \mathbf{n} = 0 \tag{6}$$

where $\partial \Delta_{ij}$ are the four cell faces intersecting orthogonally with the grid at four locations $(x_i + \Delta x/2, y_j)$, $(x_i, y_j + \Delta y/2)$, $(x_i - \Delta x/2, y_j)$ and $(x_i, y_j - \Delta y/2)$. Denoting the interface location as $\Gamma(t)$, as shown in Fig. 1, $\partial \Delta_{ij} \bigcap \Gamma(t)$ can be represented by two parts: one is the combination of the four segments of

the cell faces being cut by the interface, which can be written in the form of $A_{i+1/2,j}(t)\Delta y$, $A_{i,j+1/2}(t)\Delta x$, $A_{i-1/2,j}(t)\Delta y$ and $A_{i,j-1/2}(t)\Delta x$ where $1 \geq A \geq 0$ is the aperture; the other one is the segment of the interface $\Delta\Gamma_{i,j}(t)$ inside of the cell (i,j). Hence, Eq. (6) can be rewritten as

$$
\begin{aligned}
\left(\alpha_{i,j}^{n+1}\mathbf{U}_{i,j}^{n+1} - \alpha_{i,j}^{n}\mathbf{U}_{i,j}^{n}\right)\Delta t = & \int_{n}^{n+1} dt\frac{1}{\Delta x}\left[A_{i+1/2,j}(t)\hat{\mathbf{F}}_{i+1/2,j} - A_{i-1/2,j}(t)\hat{\mathbf{F}}_{i-1/2,j}\right] \\
& + \int_{n}^{n+1} dt\frac{1}{\Delta y}\left[A_{i,j+1/2}(t)\hat{\mathbf{F}}_{i,j+1/2} - A_{i,j-1/2}(t)\hat{\mathbf{F}}_{i,j-1/2}\right] \\
& + \int_{n}^{n+1} dt\frac{1}{\Delta x\Delta y}\hat{\mathbf{X}}\left[\Gamma_{i,j}(t)\right]
\end{aligned}
\tag{7}
$$

where $\alpha_{i,j}(t)\mathbf{U}_{i,j}$ and $\mathbf{U}_{i,j}$ are the conservative quantities in the cut cell and the cell-averaged density of conservative quantities of the considered fluid, respectively. $\hat{\mathbf{F}}$ is the average cell-face flux and $\hat{\mathbf{X}}\left[\Gamma_{i,j}(t)\right]$ is the average momentum and energy exchange across the interface segment determined by the interface interaction of Eq. (2) or (3). With explicit first-order forward time difference, the above equation can be approximated as

$$
\begin{aligned}
\alpha_{i,j}^{n+1}\mathbf{U}_{i,j}^{n+1} = & \alpha_{i,j}^{n}\mathbf{U}_{i,j}^{n} + \frac{\Delta t}{\Delta x\Delta y}\hat{\mathbf{X}}(\Delta\Gamma_{i,j}) \\
& + \frac{\Delta t}{\Delta x}\left[A_{i-1/2,j}\hat{\mathbf{F}}_{i-1/2,j} - A_{i+1/2,j}\hat{\mathbf{F}}_{i+1/2,j}\right] \\
& + \frac{\Delta t}{\Delta y}\left[A_{i,j-1/2}\hat{\mathbf{F}}_{i,j-1/2} - A_{i,j+1/2}\hat{\mathbf{F}}_{i,j+1/2}\right]
\end{aligned}
\tag{8}
$$

where Δt is the time step size. Note that all the terms on the right-hand-side are evaluated at time step n. For full cells which are not cut by an interface, volume fractions and apertures become unity and the corresponding interface segments $\Delta\Gamma_{i,j}$ vanish. Eq. (8) then simplifies to

$$
\mathbf{U}_{i,j}^{n+1} = \mathbf{U}_{i,j}^{n} + \frac{\Delta t}{\Delta x}\left(\hat{\mathbf{F}}_{i-1/2,j} - \hat{\mathbf{F}}_{i+1/2,j}\right) + \frac{\Delta t}{\Delta y}\left(\hat{\mathbf{F}}_{i,j-1/2} - \hat{\mathbf{F}}_{i,j+1/2}\right)
\tag{9}
$$

recovering a standard finite volume scheme on a two-dimensional Cartesian grid. On the other hand, since being effective only in cutting cells, Eq.(8) can also be viewed as a slight modification of Eq. (9) near the interface.

It can be found that global conservation for the considered fluid is satisfied by summing Eq. (8) over the entire domain

$$\sum_{i,j} \alpha_{i,j}^{n+1} \mathbf{U}_{i,j}^{n+1} = \sum_{i,j} \alpha_{i,j}^{n} \mathbf{U}_{i,j}^{n} + \sum_{i,j} \frac{\Delta t}{\Delta x \Delta y} \hat{\mathbf{X}}(\Delta \Gamma_{i,j}) + \text{boundary terms} \quad (10)$$

where the interface-exchange term (second term on right-hand-side) vanishes in all full cells. Note that for two-fluid problems, the evolution of each fluid is computed by solving Eq. (8) where the interface-exchange term has opposite sign. Therefore, overall conservation can be achieved by summing Eq. (10) for the two fluids

$$\sum_{k=1,2} \sum_{i,j} \alpha_{i,j}^{n+1} \mathbf{U}_{i,j}^{n+1} = \sum_{k=1,2} \sum_{i,j} \alpha_{i,j}^{n} \mathbf{U}_{i,j}^{n} + \text{boundary terms.} \quad (11)$$

Here, we make the following remarks:

- As standard Cartesian finite volume schemes are used for the discretization of differential operators, the location of the centroid of a cut cell is always approximated by the location of a grid point. This approach has been used with much success previously (Pember et al. 1995; Miller and Colella 2002).
- Whenever the volume fraction of a cut cell becomes small a mixing procedure is applied to avoid an extremely small time step.
- For higher order time integration a Runge-Kutta scheme can be employed while maintaining discrete conservation since every Runge-Kutta sub-step can be formulated as Eq. 8.
- The extension of the above formulations to three dimensions is fairly straightforward.

In the remainder of the paper we elaborate on the above ideas and implementations. The description of interface related issues can be found in Section 3. Our method is based on the level set technique. Besides the interface advection, re-initialization and state extrapolation follow previous works (Fedkiw et al. 1999; Hu and Khoo 2004). New methods are proposed to calculate the cell-face apertures and volume fractions. In Section 4 a novel but simple and low dissipation mixing procedure is introduced. In Section 5 the interface interaction terms are derived. In Section 6 the detailed implementation steps are given in the context of applications to multi-fluid and complex boundary problems, and possible extension to three dimensions. Finally, numerical examples in one and two dimensions and brief concluding remarks are given in Section 7 and Section 8, respectively.

3 Interface description

3.1 Level set function

We associate the computational domain Ω with a signed distance function $\phi(x, y, t)$, that is $\nabla|\phi| = 1$, called the level set function (Osher and Sethain 1988). Knowing ϕ we may locate the interface by finding the zero level set of ϕ. That is $\Gamma(t) = \{x, y : \phi(x, y, t) = 0\}$ which divides the entire domain into two sub-domains, each of which corresponds to a fluid or a solid body, with opposite signs of the level set function ϕ. In this paper, the aperture and volume fraction for a computational cell are defined as A^+ and α^+ for the fluid region corresponding to $\phi > 0$, while A^- and α^- for the fluid region corresponding to $\phi < 0$.

For simple geometries described with lines or circles, the initial level set function can be constructed directly by using one or more distance functions to the given curves. If more complex interfaces are considered the initial level set function is difficult to be specified analytically, and usually needs to be constructed numerically from a set of connected edges or surface patches on vertices. The first step for the construction is to determine whether a grid point is inside or outside of the interface. Many point classifications, such as the ray intersection method (Huang and Shih 1997), can be easily implemented. Next, we find a point on the interface having a minimum distance to the grid point, and designate the minimum distance and the direction to this point as the magnitude of ϕ and its normal direction, respectively.

With the level set initialized at the grid points it can be found that the continuous updating of ϕ is equivalent to the advection of the interface by the equation

$$\phi_t + u\phi_x + v\phi_y = 0 \tag{12}$$

where u and v are the velocity components for the level sets in the x and y directions, respectively. High-order schemes (Fedkiw et al. 1999; Sethain et al 2001) have been developed to solve Eq. (12). In practice, the level sets are only updated in the near interface region, which usually includes the first and second nearest cell-layers. For the region far from the interface the level sets are re-initialized (Susseman et al 1998) by the equation

$$\phi_\tau + \text{sgn}(\phi)\left(|\nabla\phi| - 1\right) = 0, \tag{13}$$

where $\text{sgn}(\phi)$ is a sign function, to maintain the signed distance property of level set function. To allow for stencil interpolation near the interface in terms

of standard finite volume schemes (Fedkiw et al. 1999) and solving for the interface conditions on grid points in near interface region (Hu and Khoo 2004), the fluid states are extrapolated to the other side of the interface by the extending equation

$$q_\tau \pm \mathbf{N} \cdot \nabla q = 0. \tag{14}$$

Here q is the extended fluid state and $\mathbf{N} \equiv (N_x, N_y)$ is the normal direction of the level set. On may note that $+\mathbf{N}$ is used to extend quantities from sub-domain with $\phi < 0$ to sub-domain with $\phi > 0$, while $-\mathbf{N}$ is used to extend quantities from sub-domain with $\phi > 0$ to sub-domain with $\phi < 0$. For a given q the extending equation can be solved until a steady solution in the near interface region is reached.

3.2 Cell-face apertures

In this paper, the cell-face apertures are calculated according to the level set distribution along the cell face. On a two-dimensional Cartesian grid, the level set function at the corners of a cell centered at (i, j) is approximated by

$$
\begin{aligned}
\phi_{i+1/2,j+1/2} &= \tfrac{1}{4} \left(\phi_{i,j} + \phi_{i+1,j} + \phi_{i,j+1} + \phi_{i+1,j+1} \right), \\
\phi_{i+1/2,j-1/2} &= \tfrac{1}{4} \left(\phi_{i,j} + \phi_{i+1,j} + \phi_{i,j-1} + \phi_{i+1,j-1} \right), \\
\phi_{i-1/2,j+1/2} &= \tfrac{1}{4} \left(\phi_{i,j} + \phi_{i-1,j} + \phi_{i,j+1} + \phi_{i-1,j+1} \right), \\
\phi_{i-1/2,j-1/2} &= \tfrac{1}{4} \left(\phi_{i,j} + \phi_{i-1,j} + \phi_{i,j-1} + \phi_{i-1,j-1} \right).
\end{aligned}
\tag{15}
$$

A sign change of the level-set function along a cell face implies that the cell face is cut by the interface. For such cells, by assuming a linear distribution of ϕ the cell-face apertures can be calculated as

$$
\begin{aligned}
A_{i+1/2,j} &= a_{i+1/2,j} \quad \text{if } \phi_{i+1/2,j+1/2} > 0 \quad \text{else } 1 - a_{i+1/2,j}, \\
A_{i-1/2,j} &= a_{i-1/2,j} \quad \text{if } \phi_{i-1/2,j+1/2} > 0 \quad \text{else } 1 - a_{i-1/2,j}, \\
A_{i,j+1/2} &= b_{i,j+1/2} \quad \text{if } \phi_{i+1/2,j+1/2} > 0 \quad \text{else } 1 - b_{i,j+1/2}, \\
A_{i,j-1/2} &= b_{i,j-1/2} \quad \text{if } \phi_{i+1/2,j-1/2} > 0 \quad \text{else } 1 - b_{i,j-1/2},
\end{aligned}
\tag{16}
$$

where $a_{i\pm1/2,j} = \frac{|\phi_{i\pm1/2,j+1/2}|}{|\phi_{i\pm1/2,j+1/2}|+|\phi_{i\pm1/2,j-1/2}|}$ and $b_{i,j\pm1/2} = \frac{|\phi_{i+1/2,j\pm1/2}|}{|\phi_{i+1/2,j\pm1/2}|+|\phi_{i-1/2,j\pm1/2}|}$. Figure 2 shows the schematic of the calculation for $A_{i+1/2,j}$. If level set does not change sign along a cell face, the aperture is either 1 (positive sign) or 0 (negative sign). Note that the above cell-face apertures, denoted as A^+, are

for the fluid region corresponding to $\phi > 0$. For the fluid corresponding to $\phi < 0$, the cell-face apertures are $A^- = 1 - A^+$.

3.3 Volume fractions

With the standard level set technique (Sussman et al. 1998), the volume fraction $\alpha_{i,j}^+$ for the fluid corresponding to $\phi > 0$ can be approximated by a smoothed Heaviside function $\alpha_{i,j}^+ = H(\phi_{i,j}, \varepsilon)$ where ε is a small positive number such as the grid size. The volume fraction α^- for the fluid corresponds to $\phi < 0$ can be calculated by the relation $\alpha^- = 1 - \alpha^+$. A simple form of the smoothed Heaviside function can be written as

$$
H(\phi, \varepsilon) = \begin{cases} 0 & \phi < -\varepsilon \\ \frac{1}{2} + \frac{\phi}{2\varepsilon} + \frac{1}{2\pi} \sin\left(\frac{\pi\phi}{\varepsilon}\right) & -\varepsilon \leq \phi \leq \varepsilon \\ 1 & \phi > \varepsilon \end{cases} \tag{17}
$$

which depends on the level set values only. By including more information on the level set normal direction a more accurate calculation for the two-dimensional volume fraction (Hu et al. 2005) can be given as

$$
H(\phi, \varepsilon) = \begin{cases} 0 & \text{if } \Lambda > \Gamma, \quad \phi < 0 \\ \frac{1}{2} + \frac{1}{\varepsilon^2} D\phi + \frac{1}{2}\frac{\Lambda^2}{\varepsilon\Gamma} & \text{if } \Gamma \geq \Lambda \geq 0, \quad \phi < 0 \\ \frac{1}{2} + \frac{1}{\varepsilon^2} D\phi & \text{if } \Lambda < 0 \\ \frac{1}{2} + \frac{1}{\varepsilon^2} D\phi - \frac{1}{2}\frac{\Lambda^2}{\varepsilon\Gamma} & \text{if } \Gamma \geq \Lambda \geq 0, \quad \phi > 0 \\ 1 & \text{if } \Lambda > \Gamma, \quad \phi > 0 \end{cases} \tag{18}
$$

in which $D = \varepsilon \min(\frac{1}{|N_x|}, \frac{1}{|N_y|})$, $\Gamma = \sqrt{D^2 - \varepsilon^2}$ and $\Lambda = \frac{\Gamma}{2} + \frac{D|\phi|}{\varepsilon} - \frac{\varepsilon}{2}$. The above smoothed Heaviside functions are symmetric to $\phi = 0$ returning a volume fraction of 0.5. In this paper, for a given fluid or a solid body, all the cells can be classified into three types: cells with volume fraction larger than 0.5 are normal cells, cells with volume fraction less than 0.5 but non-zero are small cells, and otherwise they are empty cells. Note that a normal cell for a fluid or a solid body corresponding to $\phi > 0$ is also a small or empty cell for the fluid or solid body corresponding to $\phi < 0$ and vice versa. It is noted that there are other alternative but more involved ways to calculate volume fractions according to cell-face apertures (Caiden et al. 2001). In this paper, the above simple approach is preferred for its simplicity and easy implementation. As will be shown in Section 7, for a wide range of test cases it is sufficient to produce very satisfactory results.

4   A mixing procedure

In the present method, the conservative quantities in all normal cells, small cells and newly created or vanished empty cells are updated by either Eq. (9) or (8). For a small or empty cell, a stable fluid state may not be obtained based on the time step calculated according to the full grid size CFL condition. Therefore, it is suggested that the fluid in those cells should be mixed with that of their neighboring cells. As the targeted neighboring cells are preferred to be normal cells, the mixing direction is chosen just opposite to that of the extending Eq. (14). Similarly, the targeted cells are determined from the level set normal direction. Suppose cell (i, j) is a small cell, as shown in Fig. 3, for the fluid corresponding to $\phi > 0$, the targeted cell in the x direction is chosen as cell $(i + 1, j)$ if $N_{i,j}^x > 0$ otherwise cell $(i - 1, j)$. The targeted cell in the y direction is chosen as cell $(i, j + 1)$ if $N_{i,j}^y > 0$ otherwise cell $(i, j - 1)$. For the fluid associated with $\phi < 0$, the corresponding opposite targeted cells are chosen. The changes of the conservative quantities in the x and y directions for the small cells and the targeted cells are calculated by

$$
\begin{aligned}
\mathbf{M}_{i,j}^x = -\mathbf{M}_{xtrg}^x = \frac{\beta_{i,j}^x}{\alpha_{i,j} + \alpha_{xtrg}} \left[(\alpha_{xtrg} \mathbf{U}_{xtrg}) \alpha_{i,j} - (\alpha_{i,j} \mathbf{U}_{i,j}) \alpha_{xtrg} \right] \\
\mathbf{M}_{i,j}^y = -\mathbf{M}_{ytrg}^y = \frac{\beta_{i,j}^y}{\alpha_{i,j} + \alpha_{ytrg}} \left[(\alpha_{ytrg} \mathbf{U}_{ytrg}) \alpha_{i,j} - (\alpha_{i,j} \mathbf{U}_{i,j}) \alpha_{ytrg} \right]
\end{aligned}
\tag{19}
$$

where the subscripts $xtrg$ and $ytrg$ are the indices of targeted cells in the x and y directions, respectively. Note that conservation is maintained since the conservative quantities a small cell obtained from a target cell corresponds to a loss of the target cell. The terms $\beta_{i,j}^x$ and $\beta_{i,j}^y$ are the fractions of mixing in the respective x and y directions and satisfy $\beta_{i,j}^x + \beta_{i,j}^y = 1$. A simple and robust choice is to set the fraction to 1 for the direction with larger normal direction component, that is, $\max(|N_{i,j}^x|, |N_{i,j}^y|)$. One can also choose another smoother but slightly dissipative form by defining x-direction mixing fraction as $\beta^x = |N_{i,j}^x|^2$ and y-direction mixing fraction with $\beta^y = |N_{i,j}^y|^2$. According to our numerical experiences the former gives better results for complex static boundary problems and the latter seems better suited for multi-fluid problems and complex boundary problems with moving bodies. Note that other ways to define mixing fractions are possible. It is even possible to consider the corresponding cell in the diagonal direction (for example, the cell $(i - 1, j + 1)$ in Fig. 3) as a target cell by introducing a new mixing fraction $\beta_{i,j}^{xy}$ with relation $\beta_{i,j}^x + \beta_{i,j}^{xy} + \beta_{i,j}^y = 1$ and inserting a new mixing term into Eq. 3.

After the (mixing) changes are calculated the conservative quantities for one fluid in the near interface cells are updated by

$$
\alpha_{i,j}^{n+1} \mathbf{U}_{i,j}^{n+1} = \left(\alpha_{i,j}^{n+1} \mathbf{U}_{i,j}^{n+1} \right)^* + \sum_k \mathbf{M}^x + \sum_l \mathbf{M}^y
\tag{20}
$$

where $\left(\alpha_{i,j}^{n+1}\mathbf{U}_{i,j}^{n+1}\right)^*$ are the conservative quantities at time step $n+1$ before mixing. Here, the second and third terms on the right hand side are the summations taken for all the mixing operations in the x and y directions, respectively. Actually, the indices k and l in Eq. (20) need not be determined. As the exchanges quantities at every mixing operations of Eq. (19) is accumulated for every small and target cells, one need only update these accumulated quantities once by Eq. (20) for all cells in near interface region. Easy to find that only those cells with non-vanishing exchanged quantities are effected. To avoid possible instability, only for the normal cells the fluid states are updated from cell-averaged conservative quantities. For the other cells, the corresponding fluid states are updated by the extending Eq. (14) if needed. Note that the present mixing procedure treats vanished and newly created empty cell automatically. For the former case, the residual conservative quantities are all transported to target cells and, for the latter case all the conservative quantities in a newly created small cell are transported from its target cells.

5 Interface exchanges

To obtain the momentum and energy exchanges across the interface, the proposed Riemann problems associated with interface interactions are solved on the grid points within near interface region band along the interface normal direction. With Eq. (3), for the interactions between fluid and a complex boundary the interface velocity is determined from a given prescribed or inertially coupled solid body velocity $\mathbf{v}_I = (u_I, v_I)$ by

$$\mathbf{v}_I = (\mathbf{v}_{rg} \cdot \mathbf{N})\mathbf{N}. \tag{21}$$

For problems with only weak or moderate shocks and expanding waves, simple non-iterative approximate Riemann solvers (Toro 1997) are sufficient for reasonable results, otherwise more accurate solvers are needed. In this paper, the interface condition is obtained by the interface interaction method of Hu and Khoo (2004) without modification.

After the interface interaction has been solved the interface pressure p_I and the normal velocity $\mathbf{v}_I \equiv (u_I, v_I)$ are obtained. Hence, for the fluid corresponding to $\phi > 0$, the momentum and energy transferred to it are

$$\hat{\mathbf{X}}^{\mathbf{P}}(\Delta\Gamma) = p_I \Delta\Gamma \mathbf{N}_I \quad \text{and} \quad \hat{X}^E(\Delta\Gamma) = p_I \Delta\Gamma \mathbf{N}_I \cdot \mathbf{v}_I, \tag{22}$$

respectively. Here $\Delta\Gamma$ and $\mathbf{N}_I$ are the interface segment length or area and normal direction, respectively. $\hat{\mathbf{X}}^{\mathbf{P}} = (\hat{X}_x^{\mathbf{P}}, \hat{X}_y^{\mathbf{P}})$ stands for the transferred mo-

mentum in the respective x and y directions and $\hat{X}^E$ stands for the transferred energy. In this paper, a two-dimensional approximation of Eq. (22) is used as

$$
\begin{aligned}
\hat{X}_x^{\mathbf{P}}(\Delta\Gamma_{i,j}) &= p_I(A_{i+1/2,j} - A_{i-1/2,j})\Delta x, \\
\hat{X}_y^{\mathbf{P}}(\Delta\Gamma_{i,j}) &= p_I(A_{i,j+1/2} - A_{i,j-1/2})\Delta y
\end{aligned}
\tag{23}
$$

and

$$
\hat{X}^E(\Delta\Gamma_{i,j}) = u_I\hat{X}_x^{\mathbf{P}}(\Delta\Gamma_{i,j}) + v_I\hat{X}_y^{\mathbf{P}}(\Delta\Gamma_{i,j}).
\tag{24}
$$

As shown in Fig. 4, the normalized interface segment length in the cell is approximated as

$$
\Delta\Gamma_{i,j} = \sqrt{(A_{i+1/2,j} - A_{i-1/2,j})^2 + (A_{i,j+1/2} - A_{i,j-1/2})^2}.
\tag{25}
$$

To enforce conservation the interface normal direction $\mathbf{N}_I$ in Eq. (22) is approximated with the cell-face aperture differences. Strictly, $\mathbf{N}_I$ here is not the same as the level set normal direction at the grid point $\mathbf{N}_{i,j}$ (see Fig. 4) which is also used to approximate the interface direction when solving for the interface condition for the same cell. The latter is calculated by a standard central difference from the grid point level set values and is also used to calculate cell volume fractions, extending quantities, and for mixing small cells. This apparent inconsistency can be corrected by replacing the level set normal direction with the former at these grid points. However, as both formulas are approximations with the same order, these slight differences have almost no effect on the results. Note that for the fluid corresponding to $\phi < 0$ the transferred quantities have opposite sign to that of Eqs. (23) and (24). If the interface separates two fluids the momentum and energy transferred between the two fluids have the same values but opposite sign and therefore satisfy the overall conservation property.

6 Implementation

A general procedure of the conservative interface method can be summarized as follows:

1 Given the cell-averaged density of conservative quantities $\mathbf{U}^n$ and fluid states for all grid points within normal cells, extend the fluid states to the grid points corresponding to the small or empty cells in near interface region on the other side of the interface via Eq. (14).

12

2 Solve the interface conditions on the grid points in the near interface region with the interface interaction method of Hu and Khoo (2004), and calculate the momentum and energy exchanges across the interface with Eq. (23) and (24).

3 Proceed to the next time step and compute the unmixed conservative quantities $(\alpha^{n+1}\mathbf{U}^{n+1})^*$ in all full cells and the cells in near interface region via Eq.(8).

4 Calculate the level sets ϕ^{n+1} in the near interface region for the new time step via Eq. (12) with the procedure outlined in Hu and Khoo (2004) which update the level set with interface velocity rather than the fluid velocity.

5 Re-initialize the level sets for the entire domain except the nearest region of the interface, usually the first nearest cell-layer, via Eq. (13) (details can be found in Hu and Khoo (2004)).

6 From ϕ^{n+1} calculate the cell-face aperture with Eq. (16), the level-set normal direction with standard central differences and volume fraction α^{n+1} in the near interface region by Eq. (17) or (18).

7 Invoke the mixing procedure for the small cells and newly created or vanished empty cells with Eq. (19) and (20) to obtain $\alpha^{n+1}\mathbf{U}^{n+1}$ from $(\alpha^{n+1}\mathbf{U}^{n+1})^*$.

8 Update the cell-averaged density of conservative quantities $\mathbf{U}^{n+1}$ and fluid states for all grid points within normal cells.

For multi-fluid problems, except steps 4 to 6, all steps are calculated separately for each fluid. For complex static boundary problems the steps 5 and 6 may not be necessary. If the solid body associated with the complex geometry moves with a prescribed velocity $\mathbf{v}_{rg}(t)$, the level set moves with this prescribed solid body velocity. In the case that the solid body moves by inertial coupling the solid body velocity is updated from the total momentum variation. According to Eq. (4), the average acceleration in one time step is

$$\mathbf{a}_{rg} = \frac{1}{m_{rg}} \sum_{i,j} \hat{\mathbf{X}}^{\mathbf{P}}(\Delta\Gamma_{i,j}) \tag{26}$$

and the velocity of the solid body after one time step can be obtained from

$$\mathbf{v}_{rg}^{n+1} = \mathbf{v}_{rg}^n + \mathbf{a}_{rg}\Delta t. \tag{27}$$

For higher order time accuracy a Runge-Kutta time integration can be used. In each Runge-Kutta sub-step all the above steps are invoked once, except for the re-initialization step 5 which is done only once after the last sub-step. Currently, only two-dimensional problems are considered. However, the extension of the present method to three dimensions is fairly straightforward. The only more evolved work is the calculation of cell face apertures and the approximate form of the interface surface patch $\Delta\Gamma$ for a three-dimensional cut cell.

7 Numerical examples

The following numerical examples are provided to illustrate the potential of the present interface method. For all test cases, one-phase calculations are carried out with a 5th-order WENO-LF (Jiang and Shu, 1996) and a 3rd-order TVD Runge-Kutta scheme (Shu and Osher, 1988). For one-dimensional examples, the number of grid points is 200 and the referenced exact solution, if exists, is sampled on 1000 grid points. In the two-dimensional examples, if not mentioned otherwise, the upper and lower boundaries are imposed with reflecting-wall boundary condition and the left and the right boundaries imposed with outflow boundary condition with constant extrapolation. All the computations are carried out with the CFL number of 0.6

7.1 Gas-gas interaction (I)

Case I-A: We consider a gas-gas interaction problem with the following initial conditions

$$(\rho, u, p, \gamma) = \begin{cases} (1, 0.5 \sin \left[\pi(1 - 0.5x)\right], 1, 1.4) & \text{if } x < 0.5 \\ (1, 0.5 \sin \left[\pi(1 - 0.5x)\right], 1, 1.8) & \text{if } x > 0.5 \end{cases} \tag{28}$$

and reflecting wall boundary condition applied at both $x = 0$ and $x = 1$. The case is computed up to time $t = 1$. We examine the numerical solutions with the reference "exact" solution computed with 1600 grid points. Figure 5 shows the calculated velocity and density profiles at time $t = 0, 0.25, 0.75$ and 1. At the early stage of interaction the flow, as shown in Fig. 5b and c, is continuous with primarily only expansion and compression waves transmitted across the interface. Later the flow depicts the presence of shock discontinuities, after the two compression waves have been reflected from both ends and interact with the interface and with each other (see Figs. 5c and 5d). These shock waves pass through the interface at about $t = 0.64$ and 0.80, respectively. One can observe that the computed results are in good agreement with the "exact" solution. Resolution studies are carried out to measure the numerical convergence rate of the method. For different resolutions, Fig 6 gives the variations of total entropy of the left medium $s_l = \sum_i e_i^l \alpha_i^l$, where e_i^l and α_i^l are the entropy and the volume fraction of the left medium in cell i, respectively, and of total entropy $s_T = \sum_i e_i \alpha_i$, where e_i and α_i are the entropy and volume fraction of the left or right medium in cell i, respectively. We measure the entropy errors $E_s = |s^t - s^{exact}|/s^{exact}$ at $t = 0.2, 0.64$ and 0.8 corresponding to the time when the entropy assumes the extreme value in a continuous flow or when the shock waves pass the interface. The entropy errors E_s^l and E_s^T for the left and total medium, respectively, and the averaged order of convergence R_c are

14

given in Table 1. One can find that high-order accurate results are obtained for the continuous flow. However, when there is a shock wave and especially when the shock wave passes the interface, larger errors are produced with an order of convergence decreasing towards unity.

Case I-B: We consider a well known air-helium shock tube problem with the following initial conditions

$$(\rho, u, p, \gamma) = \begin{cases} (1, 0, 1, 1.4) & \text{if } x < 0.5 \\ (0.125, 0, 0.1, 1.667) & \text{if } x > 0.5 \end{cases}. \tag{29}$$

Typical computational results at time $t = 0.15$ are shown in Fig. 7. One can find the calculated results are in reasonably good agreement with the exact solution. In particular they have almost identical and correct shock strength and speed. The interface position is also captured accurately. Note that there are larger density discrepancies near the interface (also seen in the following Case I-C) compared with to the results of Fedkiw et al (1999)(see their Fig. 8) and of Hu and Khoo (2004) (see their Fig. 3). This is because the isobaric fix used in their works produces better density profiles near interfaces. Similar treatments could also be employed in our method by modifying the states before computing the interface conditions. However, we prefer not to use the said fix since it may violate conservation considerably. As shown in Fig. 7d, the calculated interface location suggests better convergence property than that of Fedkiw et al. (1999) (see their Fig. 7 and 8), the latter shows that the interface position appears to be off by one cell for all levels of refinement as conservation at the interface is not satisfied.

We compute the relative mass and energy variations for each fluid separately during the computation by

$$V = \frac{\sum_{i=0}^{i=N} \alpha^n U_i^n \Delta x}{\sum_{i=0}^{i=N} \alpha^0 U_i^0 \Delta x}, \tag{30}$$

where U_i is the cell-averaged mass density or energy density on cell i. The superscripts n and 0 represent the nth time step and the initial condition, repectively. In a similar way, the total mass and energy variations are given as

$$V_{total} = \frac{\left[(\sum_{i=0}^{i=N} \alpha^n U_i^n)_{left} + (\sum_{i=0}^{i=N} \alpha^n U_i^n)_{right} \right] \Delta x}{\left[(\sum_{i=0}^{i=N} \alpha^0 U_i^0)_{left} + (\sum_{i=0}^{i=N} \alpha^0 U_i^0)_{right} \right] \Delta x}. \tag{31}$$

Figure 8 compares mass and energy variation of each fluid to those obtained by the interface interaction method of Hu and Khoo (2004) (denoted as I-GFM).

15

No conservation error is observed for the current method as the error is of the order of machine accuracy of 10^{-14}.

Case I-C: We compute a stiff air-helium shock tube problem, taken from Abgrall and Karni (2001) and Hu and Khoo (2004), where the initial pressure difference is much larger than that in Case I-B. The initial data are

$$(\rho, u, p, \gamma) = \begin{cases} (1, 0, 500, 1.4) & \text{if } x < 0.5 \\ (1, 0, 0.2, 1.667) & \text{if } x > 0.5 \end{cases}. \tag{32}$$

The computed results at time $t = 0.015$ are shown in Fig. 9. There is good agreement with the exact solution. At the right end of the rarefaction waves on the pressure and velocity profiles, one can observe mild overshoots which becomes significant in Abgrall and Karni (2001) (see their Fig. 6). Their scheme also produces more numerical viscosity which leads to stronger smearing of the shock front. It requires a much finer distribution of about 800 grid points for a comparably sharp shock front . Note that these overshoots are replaced by undershoots in the results of Hu and Khoo (2004) (see their Fig. 4).

Case I-D: 2D air-helium interaction In this 2-D problem, we compute a Mach 6 air shock wave interacting with a cylindrical helium bubble. Numerical computations for the same problem can be found in Bagabir and Drikakis (2001) who treat air and helium as the same fluid to avoid difficulties at the interface. For this case, the initial conditions are

$$\begin{cases} (\rho = 1, u = 0, v = 0, p = 1, \gamma = 1.4) & \text{pre-shocked air} \\ (\rho = 5.268, u = 5.752, v = 0, p = 41.83, \gamma = 1.4) & \text{post-shocked air} \\ (\rho = 0.138, u = 0, v = 0, p = 1, \gamma = 1.667) & \text{helium bubble} \\ \phi = -0.025 + \sqrt{(x - 0.15)^2 + y^2} & \text{level set} \end{cases}, \tag{33}$$

where $\phi \leq 0$ represents the helium and $\phi > 0$ represents the air, depicting a helium bubble of radius 0.025 at (0,0.15) which is to be impacted by a shock wave initiated at $x = 0.1$. The computation has been carried out with 3 increasing resolutions of $\Delta x = \Delta y = 5 \times 10^{-3}$, 2.5×10^{-3} and 1.25×10^{-3}.

Figure 10 shows the calculated density contours at 4 selected time instances ($\Delta x = \Delta y = 1.25 \times 10^{-3}$). These results show a fairly good agreement with those of Bagabir and Drikakis (their Fig. 6). The secondary reflected shock wave and triple-wave configurations are calculated with good resolution as shown in Figs 10b, c, and d. As Bagabir and Drikakis's computational model does not treat interfaces, their bubble and jet shapes are smeared and hard to identify especially after the transmitted shock wave has passed the bubble. In the present calculation these shape changes are accurately captured, including the strong instablilities at the interface which even produce

isolated air droplets in the helium bubble (see Fig. 10b and c). Also well represented is the interface after the jet collides with the downstream bubble surface which evolves to produce small separated helium pockets in the background air medium (see Fig. 10d). Another feature of the present method is that the complex topological changes is treated rather naturally without difficulty. The interface at three selected time instances is shown in Fig. 11a. It is observed that the helium bubble evolves into very complex geometries with many separated parts. In the present model, when the separated droplet/pocket becomes smaller than the grid size, the unresolved material is automatically discarded as the re-initialization procedure ignores details smaller than the grid size and reconstructs the new level sets from the resolved region. These are further shown in Fig. 11b which suggests the deleting of unresolved helium by a series of stair-step-like changes of total helium mass. Note that these mass changes happen long time after the first topological changes (at about $t = 1.1 \times 10^{-2}$) suggesting that topological changes do not violate the conservation property of the current method. Figure 11c shows the total force acting on the upper-half of the helium bubble. It is observed that second order or super-linear convergence for the peak forces before the first topological change at about $t = 1.1 \times 10^{-2}$. After the topological changes, it is hard to evaluate the convergence rate as the interface-line length is strongly dependent on interface instabilities, which suggest no simple dependency on grid sizes. Figure 11d compares the jet and upstream bubble surface trajectories calculated with different grid sizes. A second-order convergence rate is obtained by computing total relative errors between successive grid sizes.

7.2   Gas-water interaction (II)

Case II-A: Gas-water shock tube problem   This problem is taken from Hu and Khoo (2004). A real gas equation of state is used for the gas and Tait's equation of state for the water medium. The initial conditions are given as

$$(\rho, u, p, \gamma) = \begin{cases} (0.01, 0, 1000, 2) & \text{if } x < 0.5 \\ (1, 0, 1, 7.15) & \text{if } x > 0.5 \end{cases}. \tag{34}$$

In this problem the high pressure gas expands slowly comparing to the transmitted and reflected wave front speeds. Figures 12 shows the computed results at time $t = 0.0008$. Note the present results indicate slightly more accurate solutions for the rarefaction wave in gas medium and the transmitted shock wave in water than those of Hu and Khoo (2004); the latter produces a slight overshoot at the rarefaction wave and small differences in the velocity at the water-gas interface (see their Fig. 12).

Case II-B: Shock impacting on an air-water interface   We here consider the initial conditions

$$(\rho, u, p, \gamma) = \begin{cases} (1.037578, 6.0151, 1000, 7.15) & \text{if } x < 0.7 \\ (0.001, 0, 1, 1.4) & \text{if } x > 0.7 \end{cases}.$$ (35)

This is an air bubble collapse problem in one dimension. While the gas bubble collapses, the underwater shock wave impacts at the interface resulting in a weak shock wave transmitted into the air and a very strong rarefaction wave reflected back to the water medium. The calculated results at time $t = 0.003$ are shown in Fig. 13. One can find that, while in overall agreement with the exact solution, the results produced with the present method predict a more accurate pressure profile than that calculated with the interface interaction method of Hu and Khoo (2004) (denoted as I-GFM in Fig. 13). Note that the I-GFM is also a fairly robust method. As the pressure profile in Fig. 13a is plotted in logarithm scale, the oscillation produced by I-GFM is still very limited in magnitude and does not cause any stability problem. Our numerical experiments suggest that I-GFM still able to produce reasonable results although not being exactly conservative.

Case II-C: Underwater explosion   We consider an underwater explosion problem (Wardlaw and Mair 1998) in which the explosion products is modeled as a high pressure underwater gas bubble. The growth and collapse of an underwater gas bubble can be described by the one-dimensional spherically symmetric conservation laws (Leveque 1991) in which the spherical effects are taken into account as source terms. There are a number of previous simulations of this problem via arbitrary Lagrangian-Eulerian (ALE) methods (Smith 1999; Pishevar 2003; Luo et al. 2004) or an Eulerian method with a simplified model neglecting the dynamics of gas bubble and shock interface interactions (Kadioglu et al. 2005). This problem is a big challenge for any Eulerian multi-fluid method since there are very large gas bubble volume changes at a very low interface speeds which here to be computed for a very long physical time. Therefore, a very good conservation property is crucial to predict this phenomenon correctly.

The initial conditions for this problem are

$$(\rho, u, p, \gamma) = \begin{cases} (1.63, 0, 83810, 1.4) & \text{if } 0 < x < 0.16 \\ (1.025, 0, 10, 5.5) & \text{if } 400 > x > 0.16 \end{cases}.$$ (36)

and which are taken from Pishevar (2003). The reflecting wall boundary condition is used for the left boundary. We do not implement a boundary condition to the right boundary as the disturbance does not arrive there in the calculations. As in Pishevar (2003) a stiff gas equation of state is used for water, i.e. $(\gamma - 1)\rho e = p + \gamma p_0$ where $\gamma = 5.5$ and $p_0 = 4921.15$. To obtain a mesh con-

18

verged bubble oscillation period the calculation is performed with grid sizes of $\Delta x = 0.2, 0.1, 0.05, 0.025$ and 0.0125, corresponding to 0.8, 1.6, 3.2, 6.4 and 12.8 grid points (computational cells) for the initial gas bubble of 16cm radius.

Figure 14 shows the calculated bubble radius and interface pressure history with different grid sizes, both of which suggest a second-order convergence rate. The converged results, such as a bubble oscillation period of about 0.2s and a maximum bubble radius at about 3m at time $t = 0.1$ms, are in good agreement with previous ALE calculation (Pishevar 2003). Our results also show pressure oscillations at the interface which has been found in previous works (Mader 1979; Wardlaw and Mair 1998; Luo et al. 2004). Note that the current calculations capture correct physics with much fewer grid point for the gas bubble than previous ALE simulations. Further calculations (not shown here) suggest that when Tait's equation is used for the water medium, almost identical results are obtained with a slightly larger oscillation period. In the present computations the so called "jaggedness" (or oscillatory behavior with limited magnitude) phenomena with complex secondary, tertiary and more successive shock waves produced by interface interactions can be captured clearly when the gas bubble is described with similarly high numerical resolution as previous ALE simulations. Figure 15 depicts the "jaggedness" phenomena at the early stage of the interaction when approximately 600 grid points are used for the gas bubble. Again, these results are in very good agreements with previous ALE simulations (Smith 1999; Pishevar 2003; Luo et al 2004).

Case II-D: Collapse of 2D air bubbles in water   We consider the interactions between two neighboring 2D bubbles and a strong shock wave. This problem has been previously simulated by Hankin (2001): two, 6mm and 3mm diameter cylindrical air bubbles in water are impacted by a 1.6GPa shock wave. According to Hankin (2001), the schematic of the problem is given in Fig. 16a which shows a $15 \times 15mm$ computational domain. The initial data are

$$\begin{cases} (\rho = 1, u = 0, v = 0, p = 1.013, \gamma = 7.15) & \text{pre-shocked water} \\ (\rho = 1.226, u = 54.28, v = 0, p = 16000, \gamma = 7.15) & \text{post-shocked water} \\ (\rho = 1.2 \times 10^{-3}, u = 0, v = 0, p = 1, \gamma = 1.4) & \text{air bubble} \\ \phi = -3 + \sqrt{(x - 7.5)^2 + (y - 8.5)^2} & \text{level set for } y > -x + 11.5 \\ \phi = -1.5 + \sqrt{(x - 3.75)^2 + (y - 5)^2} & \text{level set for the rest region} \end{cases} .(37)$$

Here $\phi \leq 0$ represents the air and $\phi > 0$ represents the water. Initially, the shock wave just reaches the small air bubble. 150×150 grid points, approximately the same as in Hankin (2001), are used for the computations. Figures 16b, 16c and 16d show the typical density contours at $t = 0.18(1.8\mu s)$, $t = 0.34(3.4\mu s)$ and $t = 0.46(4.6\mu s)$ which depict good agreement with those

of Hankin (2001) (their Fig. 5). One can find that, although even slightly less grid points have been used in the present calculation the shapes of the bubbles are captured in much more detail. Note that when the small bubble is split by jets and compressed to a scale smaller than the grid size it vanishes and affects the rest flow field no more. Furthermore, after the small bubble has collapsed and vanished the explosion waves originating from these collapse points (see Fig. 16c) lead to two cavitation regions. Since the present model does not include any cavitation model the computation is stopped when in these regions eventually a negative sound speed arises.

7.3 Complex boundary problems (III)

Case III-A: Moving wall problem   We consider a gas confined between two reflecting walls at $x_l = 0$ and $x_r = 0.5 + u_r t$ with constant $u_r = 0.5$. The initial conditions are

$$[\rho(x), u(x), p(x)] = \left[1 + 0.2\cos(\pi - 2\pi x), 2u_r(1 - x), \rho(x)^{1.4}\right] \qquad (38)$$

in which the entropy $s(x) = 1$. This problem is taken from Forrer and Berger (1998). We examine the numerical solutions and comparing to the reference "exact" solution computed with 1600 grid points. We calculate this case to time $t = 0.6$. Figure 17 presents the results at time $t = 0, 0.2, 0.4$ and 0.6. One can observe that the computed results are in quite good agreement with the "exact" solution. Note that the grid points occupied by the wall are filled with zeros. Resolution studies are also carried out to measure the numerical convergence rate of the method. Since the analytic solution is smooth the entropy stays constant throughout. We examine the total entropy error err_{ttl} calculated by $err_{ttl} = \sum_j |s_j^{final} - 1|\alpha_j^{final} / \sum_j \alpha_j^0$ and the entropy error on the moving boundary given by $err_{bry} = |s_I^{final} - 1|$, respectively, at the final time. Table 2 shows the an error analysis of the above errors, which gives a second-order convergence rate for the total error and a slightly better than linear convergence rate for the boundary error. These results are in good agreement with Forrer and Berger (1998) and Arienti et al. (2003) using non-conservative methods.

Case III-B: Shock diffraction on an airfoil   We consider a Mach 1.5 shock wave diffraction on a NACA0018 airfoil with $+30^o$ angle of attack. Numerical computations for the similar problem with Cartesian grid can be found in Yang et al. (1997a) with the grid intersection method and Ripley et al (2003) with an immersed boundary method. The present set-up of the problem is the same as in Yang et al. (1997a) where a 1.8×2 computational domain is

employed. The initial data are

$$\begin{cases} (\rho = 1.4, u = 0, v = 0, p = 1.0, \gamma = 1.4) & \text{pre-shocked air} \\ (\rho = 2.607, u = 0.694, v = 0, p = 2.4583, \gamma = 1.4) & \text{post-shocked air} \end{cases} \quad .(39)$$

The level set is built from a polyline consisting of 200 control points (Hu et al. 2005). Figure 18a shows the computed results on a 360×400 grid at time $t = 0.64$ which suggests a good agreement with the shock structure from the experimental results of Mandella and Bershader (1987) at an approximately similar time. Compared with the results of Ripley et al (2003) obtained with a 500×500 grid, the present method shows higher order accuracy by which a much sharper shock wave front and refined flow structures near the airfoil head and tip are produced. Note that the discontinuities near the solid body are sharply predicted which eliminates the problems associated with artificial numerical boundary layer found in Quirk (1994) and Yang et al (1997a). By imposing the free stream velocity and density with the post-shock values we calculate the lift and drag coefficients by $C_l = \frac{F_y}{\frac{1}{2}\rho_\infty u_\infty^2 L}$, $C_d = \frac{F_x}{\frac{1}{2}\rho_\infty u_\infty^2 L}$ where F_x and F_y are the total momentum exchange rate integrated along the boundary in the x and y directions, respectively, and L is the airfoil chord length. The calculated lift and drag coefficients with different grid sizes are shown in Fig. 18b which suggest about second-order convergence rate for the peak lift coefficient and linear convergence for the drag coefficient.

Case III-C: The liftoff of a cylinder by a shock wave This example of a flow with complex moving boundary is taken from Falcovitz et al (1997) on the liftoff of a cylinder by a shock wave. A rigid light-weight cylinder, initially resting on the lower wall of a two-dimensional channel, is driven and lifted upwards by a Mach 3 shock wave. The problem has also been simulated with non-conservative methods by Forrer and Berger (1998) and by Arienti et al. (2003) which implement the moving boundary condition with mirror or injection operations. The initial data for this problem is

$$\begin{cases} (\rho = 1, u = 0, v = 0, p = 1) & \text{pre-shocked air} \\ (\rho = 3.857, u = 2.629, v = 0, p = 10.333) & \text{post-shocked air} \\ \phi = -0.05 + \sqrt{(x - 0.15)^2 + (y - 0.05)^2} & \text{level set} \end{cases} \quad . \quad (40)$$

Here, $\phi \le 0$ represents the cylinder with a radius of 0.05 and density of 7.6 and $\phi > 0$ represents the air in the channel. The computational domain is 1.0×0.15, for which the left inlet boundary assumes the post-shock parameters. Different grid sizes of $\Delta x = \Delta y = 2.5 \times 10^{-3}$, 1.25×10^{-3} and 6.25×10^{-4} are used. Figure 19 shows the pressure contours at three different times $t = 0.0, 0.014$ and 0.0255, which correspond to times $t = 0, 500$ and 910 of Falcovitz et al (1997), respectively. Our results show that at time $t = 0.028$ ($t = 1000$ in Falcovitz et al (1997)) the cylinder has already left the top boundary of the

21

domain. These results agree with Forrer and Berger (1998) and Arienti et al. (2003). A strong vortex appears under the cylinder in the results of Forrer and Berger (1998) (see their Fig. 5). However, as shown in Fig. 19b and c, this vortex can not been found here. The same phenomenon is found after we have examined our low resolution results (not shown here) and the results in Arienti et al. (2003) (their Fig. 19). One possible reason for this discrepancy may be caused by the space-time splitting scheme employed in Forrer and Berger (1998). The different treatment of the tangential direction velocities for the ghost nodes may effects the numerical dissipation considerably. In the present results, the measured cylinder centers at $t = 0.0255$ with increasing resolution are (0.659, 0.132), (0.649, 0.145) and (0.641, 0.147), corresponding grid sizes are $\Delta x = \Delta y = 2.5 \times 10^{-3}$, 1.25×10^{-3} and 6.25×10^{-4}. There results imply a super-linear convergence rate, slightly better than that of Arienti et al. (2003). This is perhaps to be expected since the present conservative interface method may improve the solution especially when the calculation is carried out on long time scales.

8 Concluding remarks

In this paper, we have developed a conservative interface method suitable for both multi-fluid problems and complex boundary problems. The conservation property removes or reduces any conservative associated errors especially when there are strong or long physical time scale interactions across the interface. As the method is constructed based on a standard Cartesian finite volume method and level set technique, it maintains the simplicity of GFM-like methods for implementation and handles topological changes naturally. The present method also offers a fairly simple way of implementation in multi-dimension and for multi-level time integrations without space-time splitting. A number of numerical examples in one dimension are studied with comparisons to exact solutions while two dimensional problems are calculated and compared to experiments and results of previous works. The obtained results suggest that the present method exhibits a large degree of robustness and accuracy with quite good convergence properties. As the different types of interface problems in this work are treated with the same approach our method may provide a way towards universal methods for interface problems.

References

[1] Abgrall R and Karni S (2001) Computations of compressible multifluids. *J. Comput. Phys.* **169** 594-623

[2] Arienti R, Hung P, Morano E, Shepherd JE (2003) A level set approach to Eulerian-Lagranian coupling. *J. Comput. Phys.* **185**, 213 (2003)

[3] Bagabir A and Drikakis D (2001) Mach number effects on shock-bubble interaction. *Shock Waves* **11** 209-218

[4] Benek JA, Donegan TL, Steger JL (1987) Extended chimera grid embeding scheme with application to viscous flows. *AIAA paper* **No.** 87-1126

[5] Berger MJ, LeVque RJ (1989) An adaptive Cartesian Mesh algorithm for the Euler equations in arbitrary geometries. *AIAA paper* **No.** 89-1930

[6] Caiden R, Fedkiw RP, Anderson C (2001) A Numerical Method for Two-Phase Flow Consisting of Separate Compressible and Incompressible Regions. *J. Comput. Phys.* **166**, 1-27

[7] Chiang YL, van Leer B, Powell KG (1992) Simulation of unstady inviscid flow on an adaptively refined Cartesian grid. *AIAA paper* **No.** 92-0443

[8] Chung MH (2001) A level set approach for computing solutions to inviscid compressible flow with moving solid boundary using fixed Caresian grids. *Int. J. Numer. Meth. Fluids* **33** 1121-1151

[9] Colella P (1990) Multidimensional upwind method for hyperbolic conservation laws. *J. Comput. Phys.* **87** 171 - 200

[10] Davis SF (1992) An interface tracking method for hyperbolic systems of conservation laws. *Appl. Numer. Math.* **10** 447-472

[11] Falcovitz J, Alfandary G, Hanoch G (1997) A two-dimensional conservation laws schemes for compressible flows with moving boundaries. *J. Comput. Phys.* **72** 449-466

[12] Fedkiw R, Aslam T, Merriman B and Osher S (1999) A non-oscillatory Eulerian Approch to interfaces in multimaterial flows (the ghost fluid method). *J. Comput. Phys.* **152** 457-492

[13] Forrer H, Berger M (1998) Flow simulation on Cartesian grids invloving complex moving geometries flows. In: *Int. Ser. Numer. Math., 129, Birkhäuser, Basel*

[14] Forrer H and Jeltsch (1998) A High-order boundary treatment for Cartesian-grid method. *J. Comput. Phys.* **140**, 259-277

[15] Glimm J, Marchesin D and McBryan O (1981) A numerical method for two phase flow with an unstable interface. *J. Comput. Phys.* **39** 179-200

[16] Glimm J, Li X, Liu Y, Xu Z, Zhao N (2003) Conservative front tracking with improved accuracy. *SIAM J. Numer. Anal.* **39** 179-200

[17] Hankin RS (2001) The Euler equations for multiphase compressible flow in conservation form: simulation of shock-bubble interactions. *J. Comput. Phys.* **172**, 808-826

[18] Hirt CW and Nichols BD (1981) Volume of fluid (VOF) method for the dynamics of free boundaries. *J. Comput. Phys.* **39** 201

[19] Hirt CW (1993) Volume-fraction techniques: powerful tools for wind engineering. *J. Wind Engrg. & Industr. Aerodyn.*, **46-47** 327-338

[20] Hu XY, Khoo BC (2004) An interface interaction method for compressible multifluids. *J. Comput. Phys.* **198**, 35-64

[21] Hu XY, Khoo BC, Adams NA (2005) A smoothed interface interaction method for compressible flow. In: *The 25th International Symposium on Shock Waves , Bangalore, July 17 - 21, India, 2005*

[22] Huang CW, Shih TY (1997)On the complexity of point-in-polygon algorithms. *Computers and Geosciences* 23, 109-118

[23] Jameson A, Baker, TJ, Weatherill, NP (1986) Calculation of inviscid transonic flow over a complete aircraft. *AIAA paper* **No.** 86-0103

[24] Jiang GS and Shu CW (1996) Efficient Implementation of Weighted ENO Schemes. *J. Comput. Phys.* **126** 202-228

[25] Kadioglu SY, Sussman M, Osher S, Wright JP, Kang M (2005) A second order primitive preconditioner for solving all speed multi-phase flows. *J. Comput. Phys.* **209** 477-503

[26] Leveque RJ (1991) *Numerical method for conservation laws* Birkhauser, Verlag

[27] Liu TG, Khoo BC and Yeo KS (2003) Ghost fluid method for strong shock impacting on material interface. *J. Comput. Phys.* **190** 651-681

[28] Löhner R (1987) The efficient simulation of strong unsteady flows by finite element method. *AIAA paper* **No.** 87-0555

[29] Luo H, Baum JD, Löhner R (2004) On the computation of multi-material flows using ALE formulation. *J. Comput. Phys.* **194** 304-328

[30] Mader C (1979) *Numerical modeling of detonation.* University of California Press, Los Angeles

[31] Mandella M, Bershader D (1987) Quantitative Study of Compressible Vortices: Generation, Structure and Interaction with Airfoils. *AIAA paper No. 87-0328*

[32] Miller GH, Colella P (2001) A conservative three-dimensional Eulerian method for coupled solid-fluid shock capturing. *J. Comput. Phys.* **183** 26-82

[33] Nguyen D, Gibou F and Fedkiw R (2002) A fully conservative ghost fluid method and stiff detonation waves. *12th International Detonation Symposium, San Diego, CA*

[34] Osher S and Sethain JA (1988) Front propagating with curvature dependent speed: algorithm based on Hamilton-Jaccobi formulation. *J. Comput. Phys.* **79** 12-49

[35] Pember RB, Bell JB, Colella P, Crutchfield WY, Welcome ML (1995) An Adaptive Cartesian Grid Method for Unsteady Compressible Flow in Irregular Regions. *J. Comput. Phys.* **120** 228-304

[36] Peraire J, Vahdati M, Morgan K, Zienkiewicz OC (1987) Adaptive remeshing for compressible flow computations. *J. Comput. Phys.* **72** 449-466

[37] Pishevar AR (2003) An ALE Method for Compressible Multifluid flows: Application to Underwater Explosion . In: *CFD2003, Vancouver, May 28-30, Cananda, 2003*

[38] Quirk JJ (1994) An alternative to unstructured grid for computing gas dynamic flows around arbitrarily complex two-dimensional bodies. *Computers Fluids* **23** 125-142

[39] Ripley RC, Whitehouse DR, Lien FS: Effect of mesh topology on shock wave loading computations. In: *CFD2003, Vancouver, May 28-30, Cananda, 2003*

[40] Sethain JA (2001) Evolution, implementation, and application of level set and fast marching methods for advancing fronts. *J. Comput. Phys.* **169** 503-555

[41] Shu CW and Osher S (1988) Efficient implementation of essentially non-oscillatory shock-capturing schemes. *J. Comput. Phys.* **77** 439-471

[42] Smith RW (2001) AUSM(ALE): A Geometrically Conservative Arbitrary Lagrangian-Eulerian Flux Splitting Scheme . *J. Comput. Phys.* **150** 268-286

[43] Sussman M, Fatemi E, Smereka P, Osher S (1998) An impoved level set method for incompressible two-phase flows. *Comp. & Fluids* **27** 663-680

[44] Toro EF (1997) *Riemann solvers and numerical methods for fluid dynamics: a practical introduction.* Berlin; New York, Springer

[45] Wardlaw AB, Mair HU (1998) Spherical solutions of an underwater explosion bubble. *Shock and Vibration* **5** 89 - 102

[46] Yabe T, Xiao F, Utsumi T (2001) The constrained interpolation profile method for multiphase analysis. *J. Comput. Phys.* **169** 556-593

[47] Yang G, Causon DM, Ingram DM, Saunders R, Batten P (1997a) A Cartesian cut cell method for compressible flows Part A: static body problems. *Aeronautical Journal* **101** 47-56

[48] Yang G, Causon DM, Ingram DM, Saunders R, Batten P (1997b) A Cartesian cut cell method for compressible flows Part B: moving body problems. *Aeronautical Journal* **101** 57-65

[49] Youngs DL (1982) Time-dependent multi-material flow with large fluid distortion, in Numerical Methods for Fluid Dynamics. edited by K. W. Morton and M. J. Baines, Academic Press, New York, p.273

List of Figures

26

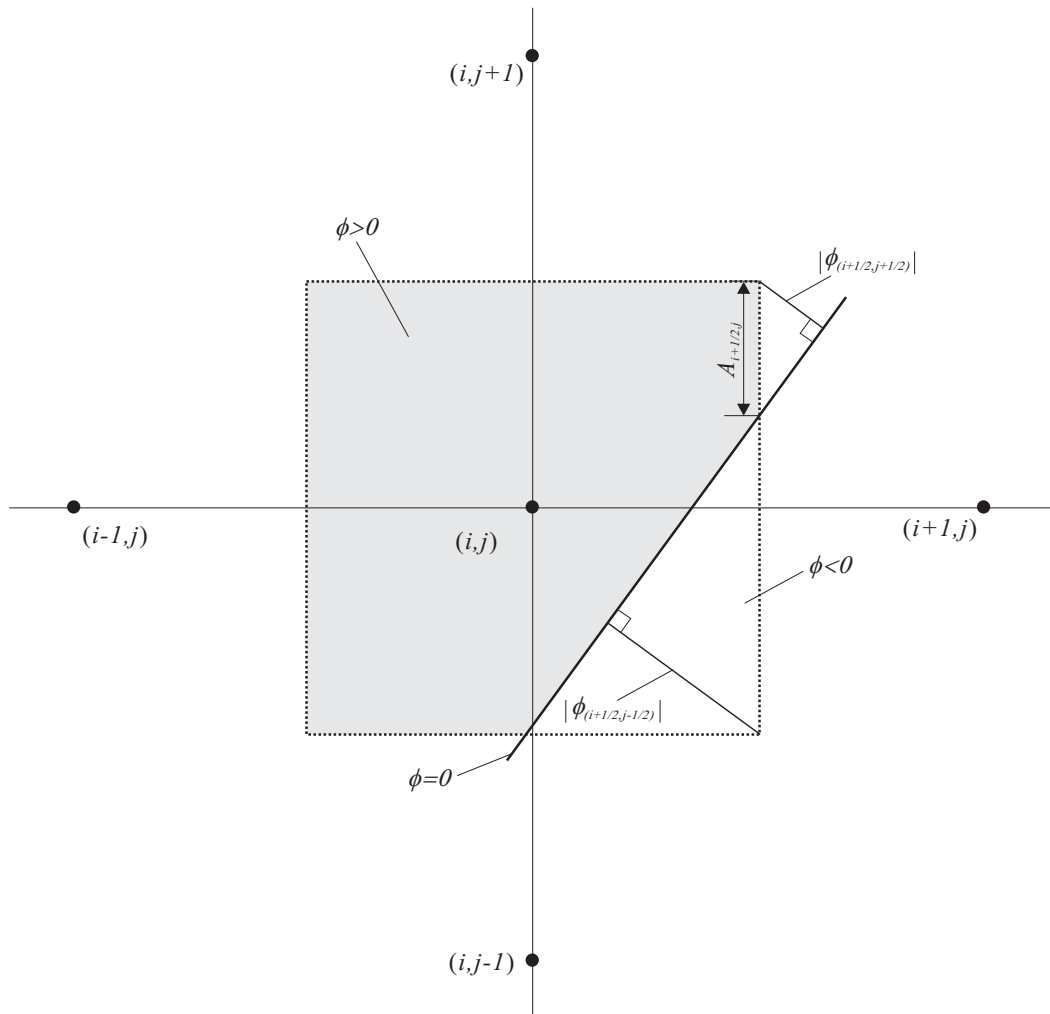Fig. 1. Schematic of conservative discretization for a cut cell.

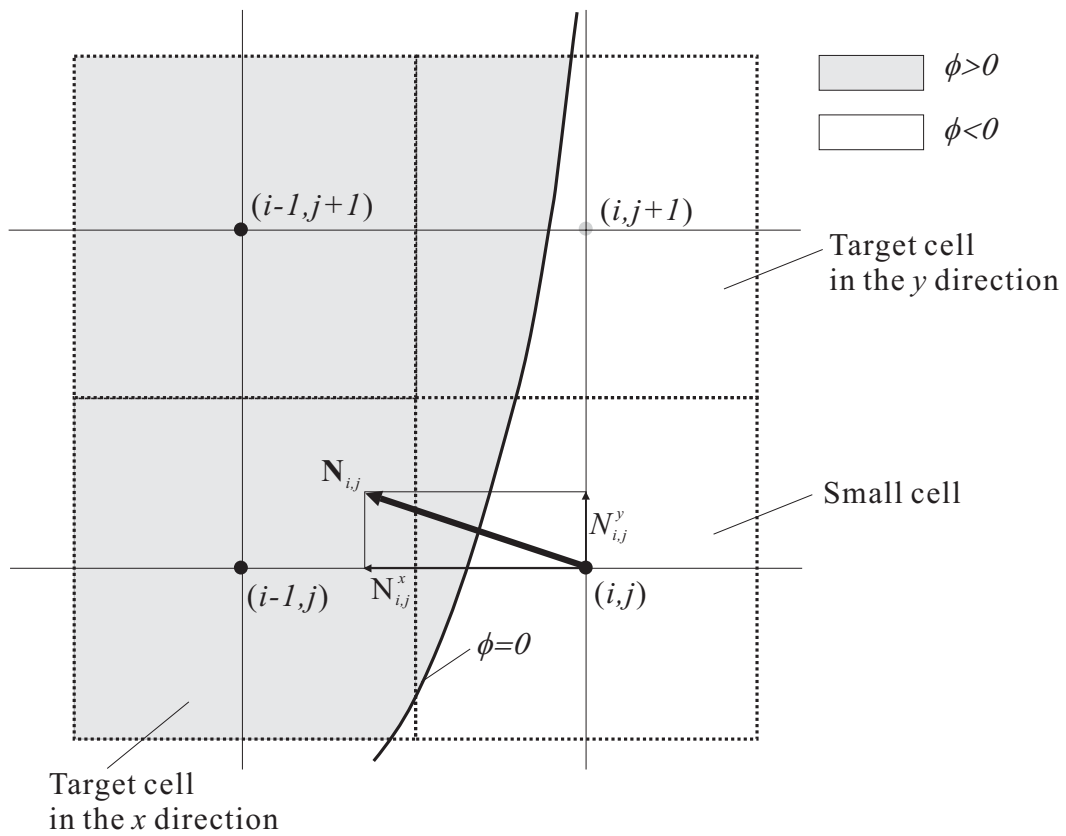Fig. 2. The calculation of the aperture $A_{i+1/2,j}$.

Fig. 3. The target cells for a small cell of fluid corresponding to $\phi > 0$.
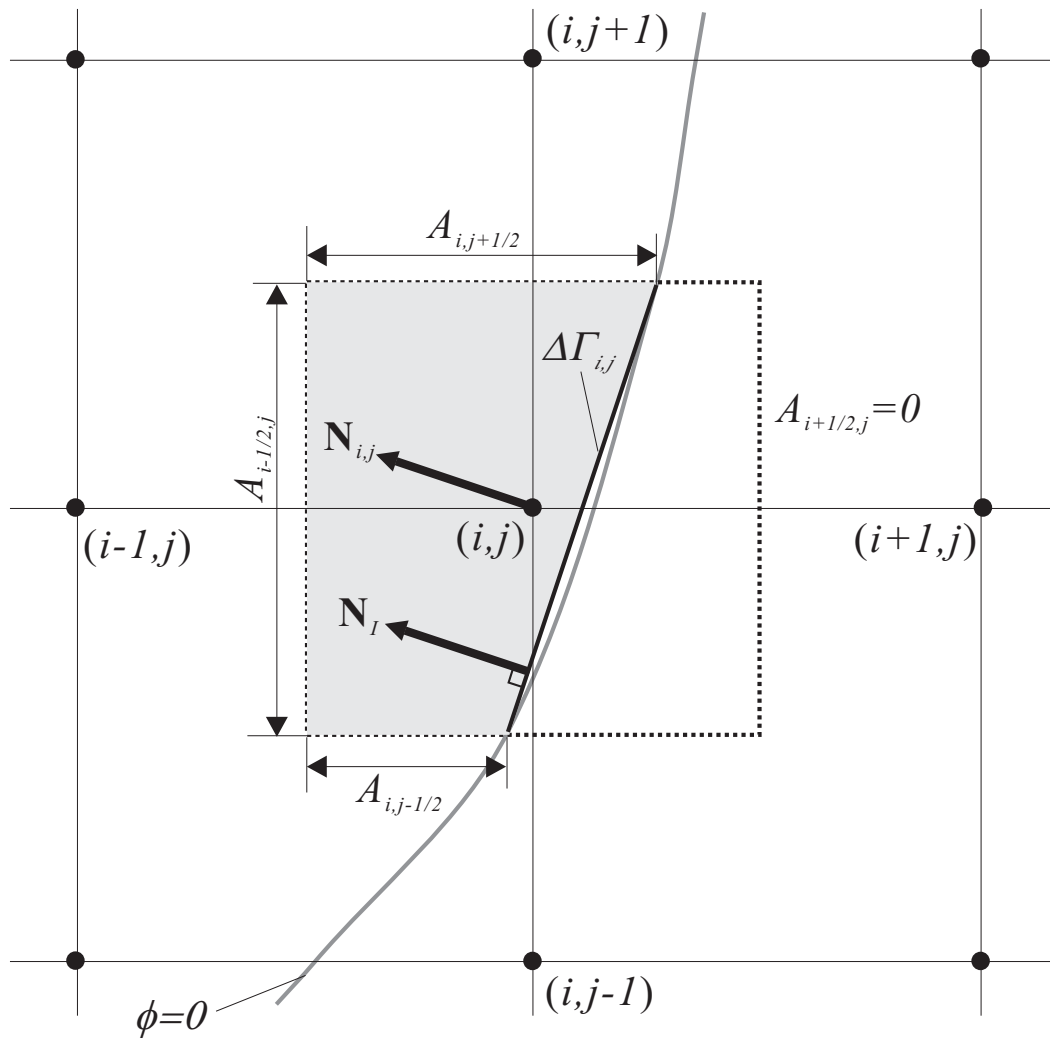
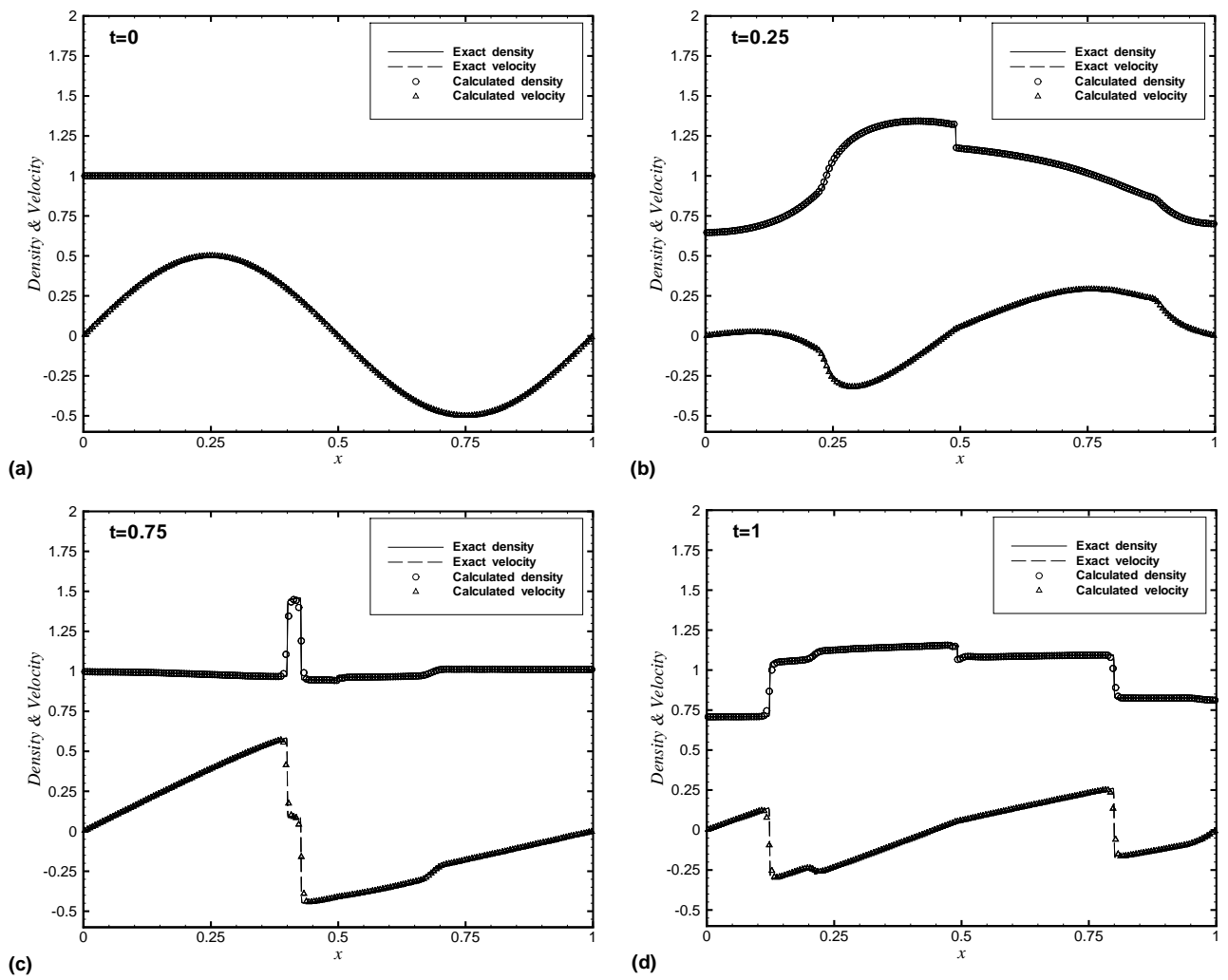Fig. 4. Schematic of conservative discretization for a cut cell
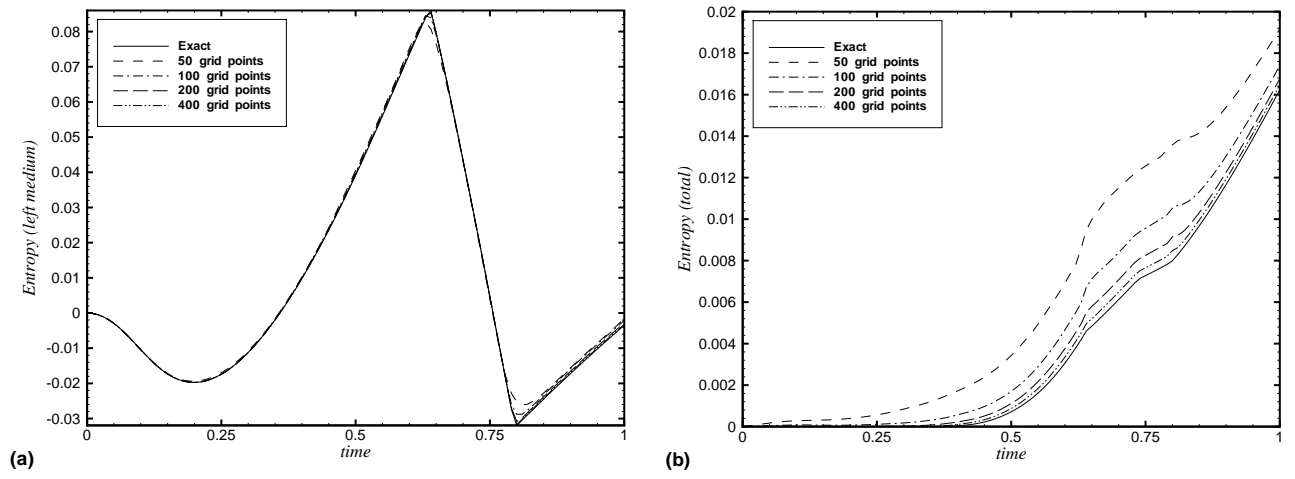
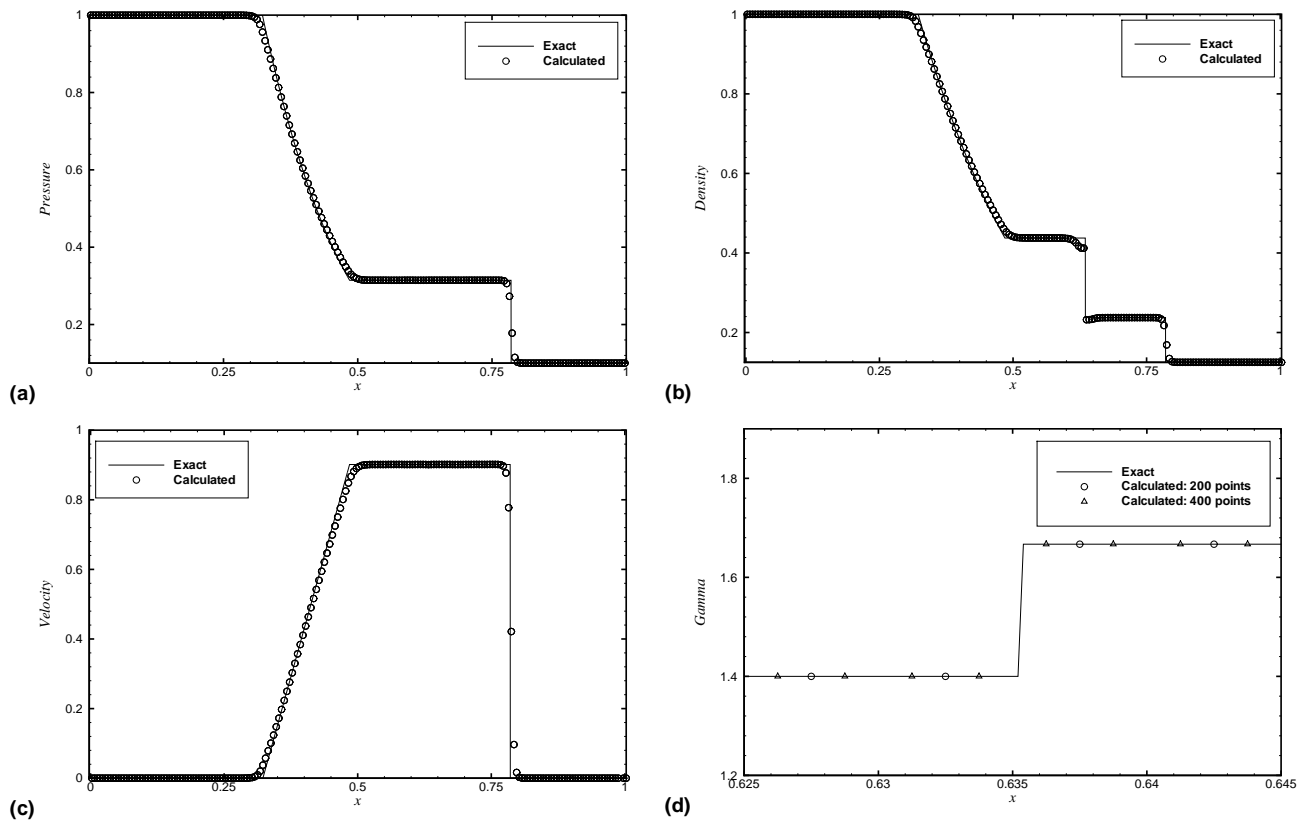Fig. 5. Gas-gas interaction: Case I-A.

Fig. 6. Case I-A: convergence test.
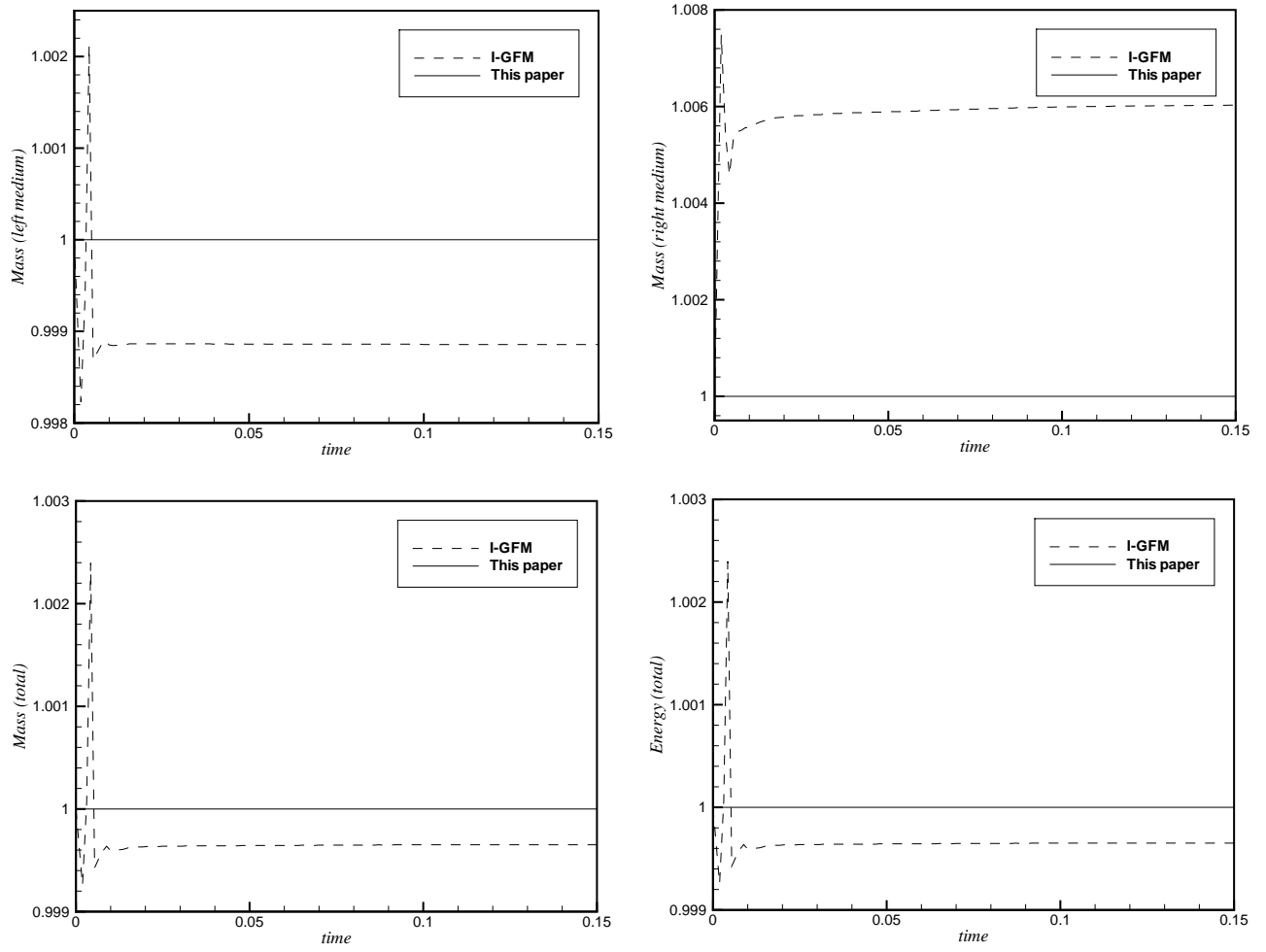
Fig. 7. Case I-B: air-helium shock tube problem.
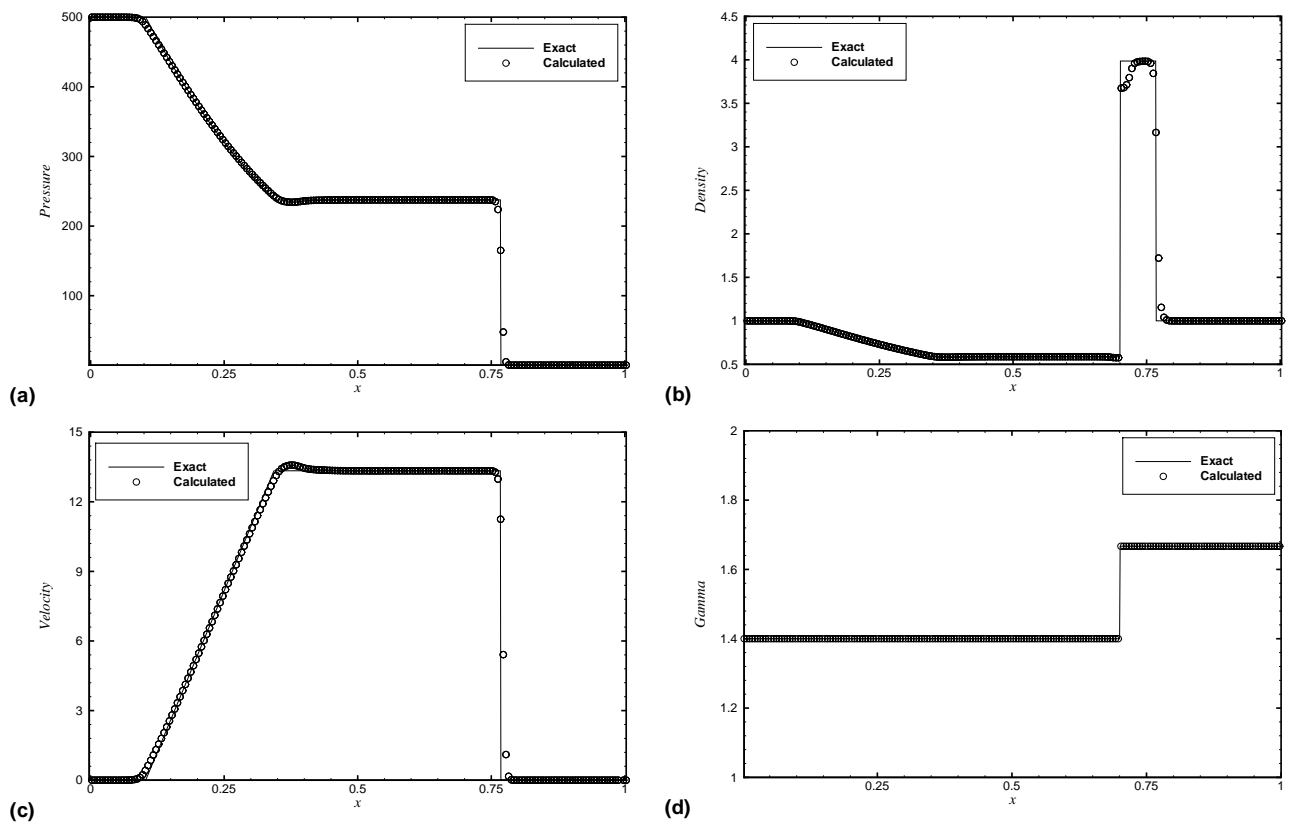
34

Fig. 8. Case I-B: conservation test.

(a)

(b)

(c)

(d)

Fig. 9. Case I-C: stiff air-helium shock tube problem.

36
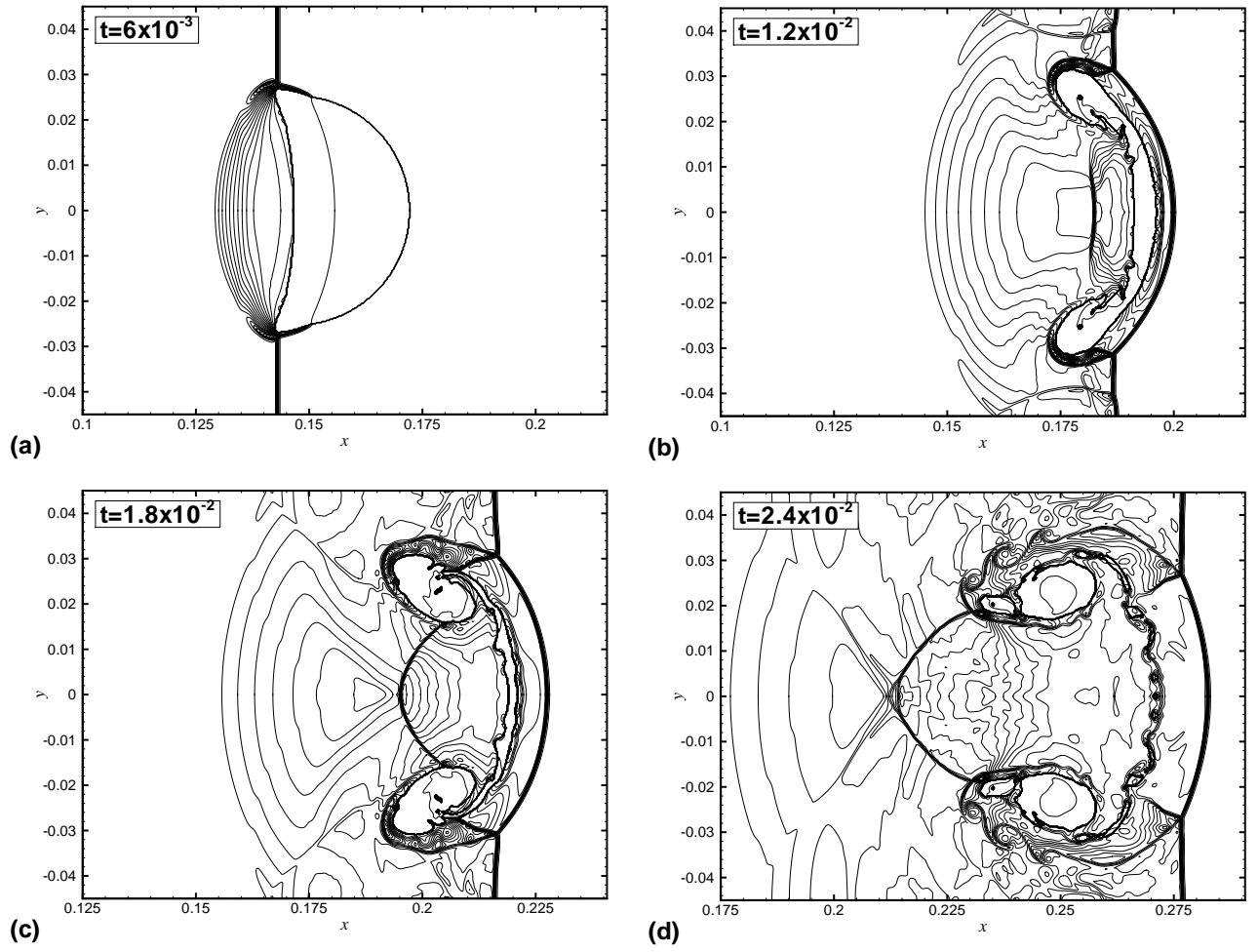
Fig. 10. Case I-D: 35 contours of density, from 0 to 9 for selected time instances.

37
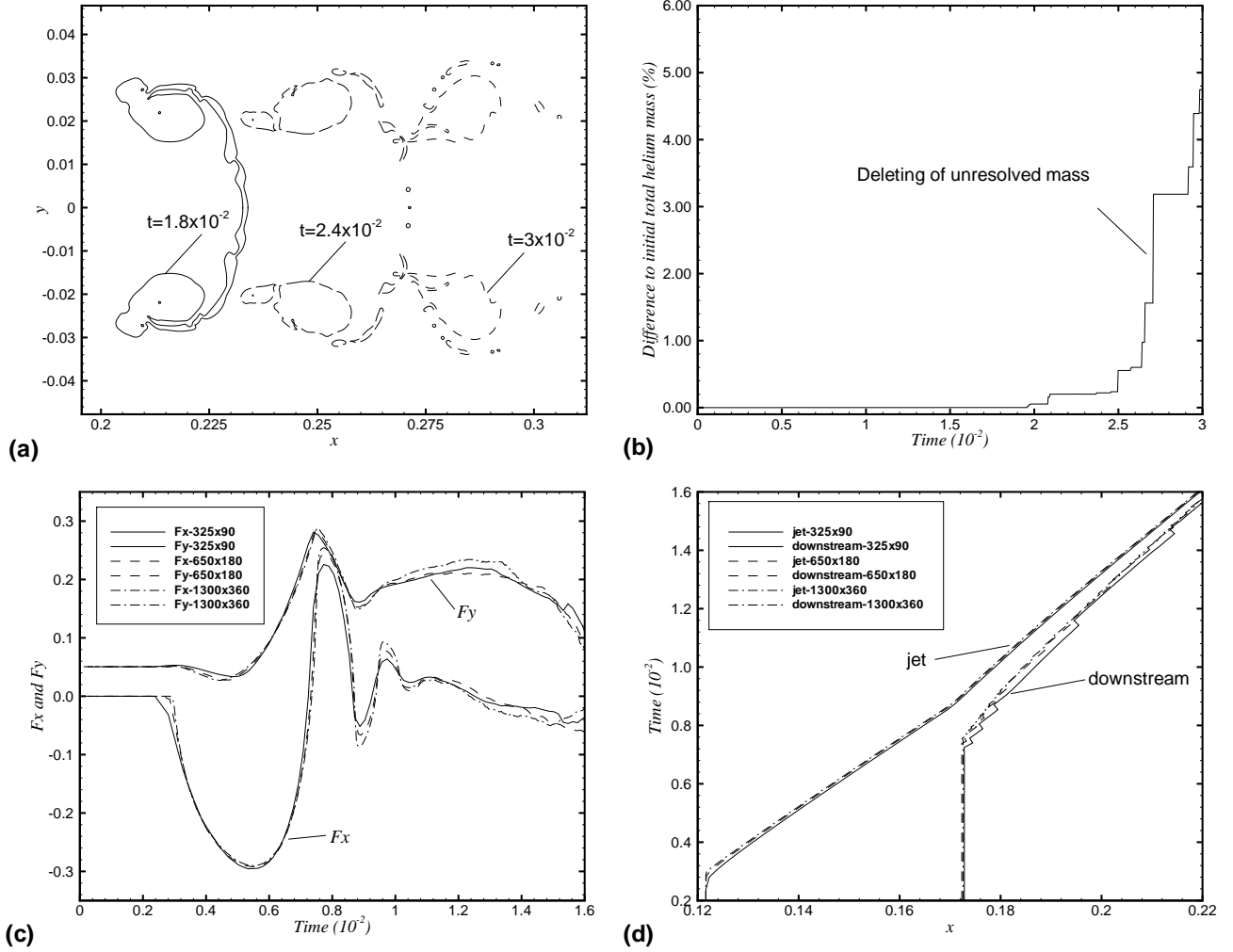
Fig. 11. Case I-D: (a) interfaces at three selected time instances, (b) time variation of the difference between total helium mass to its initial value, (c) forces on the upper-half of the helium bubble with different grid sizes, (d) jet and downstream bubble surface trajectories with different grid sizes.

38
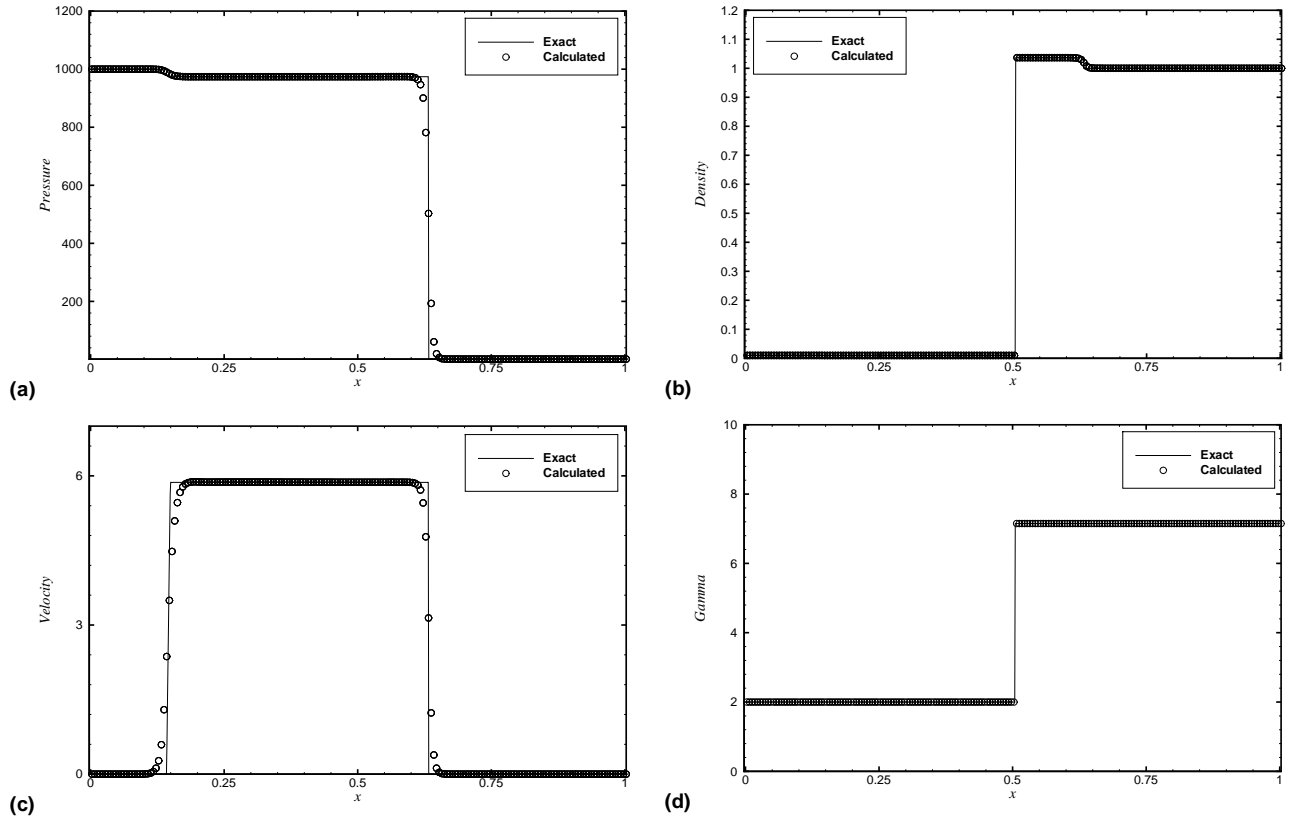
Fig. 12. Case II-A: gas-water shock tube problem

39
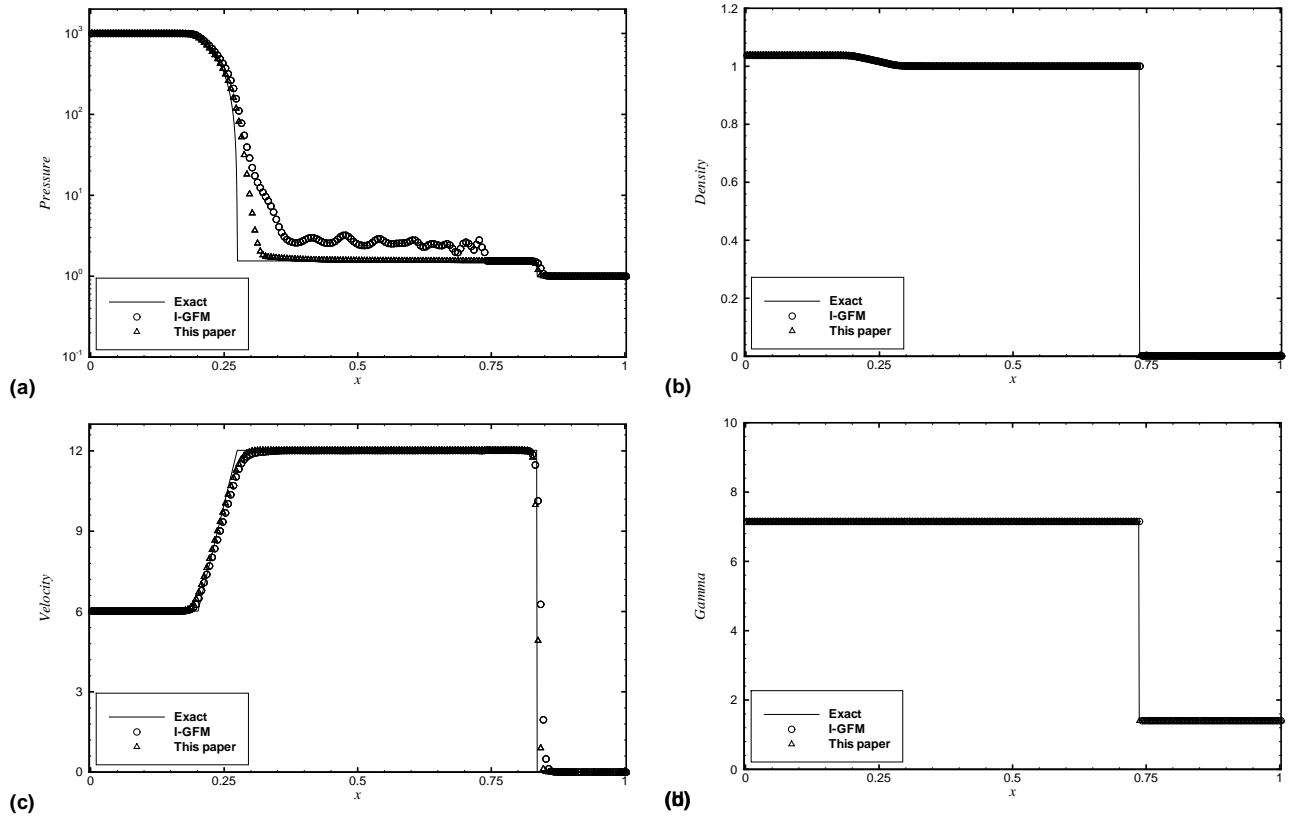
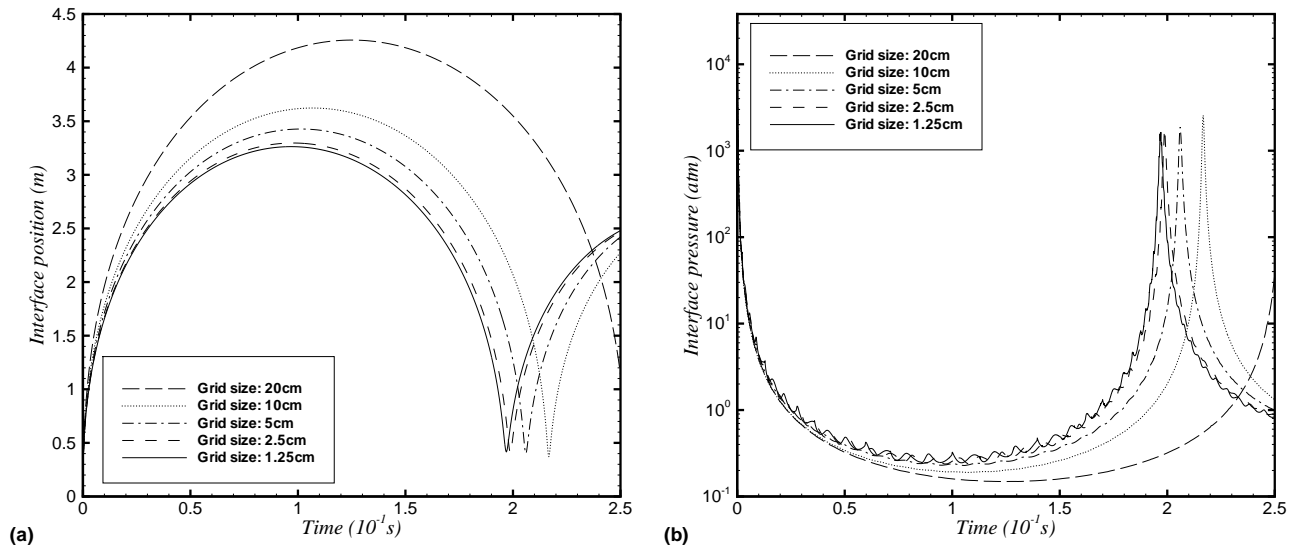Fig. 13. Case II-B: shock impacting air-water interface.

40

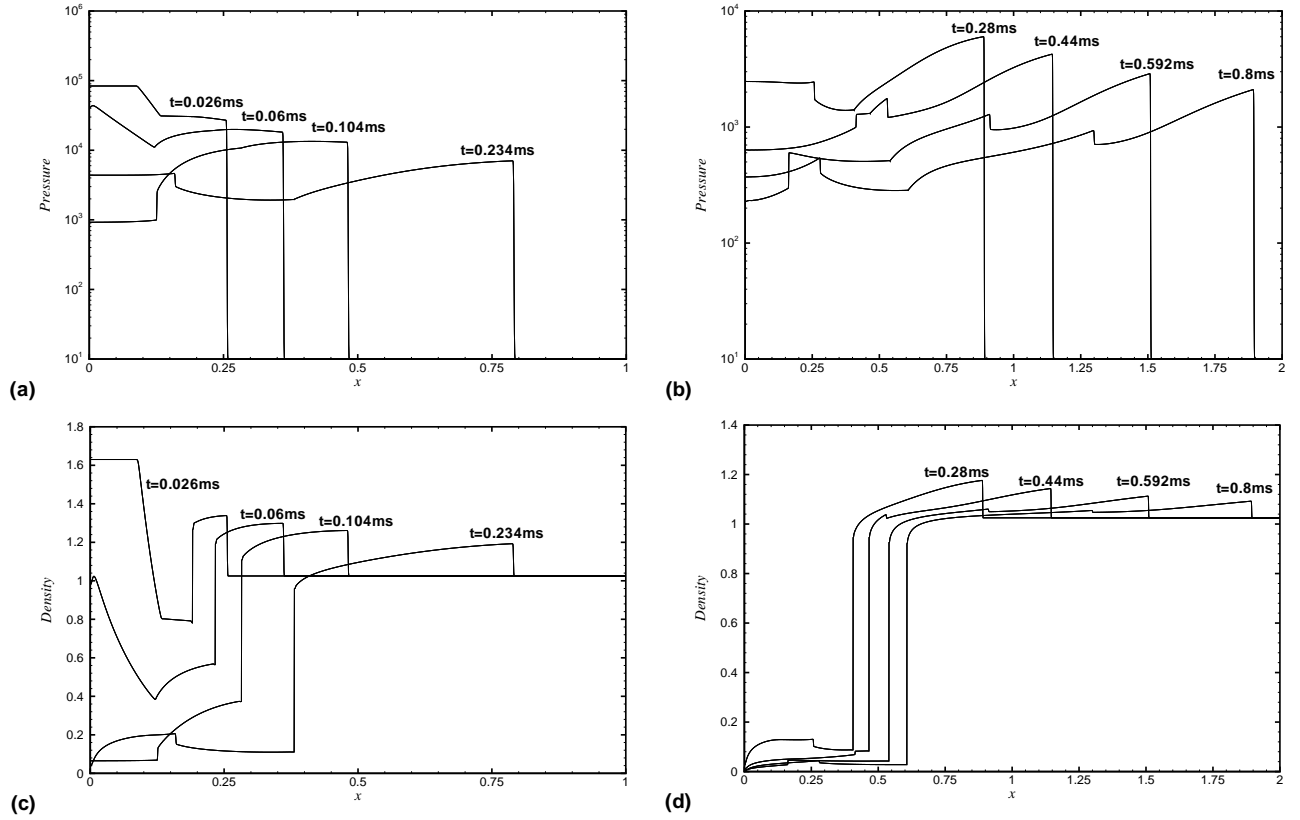Fig. 14. Case II-C: bubble radius time and interface pressure history for different grid sizes.

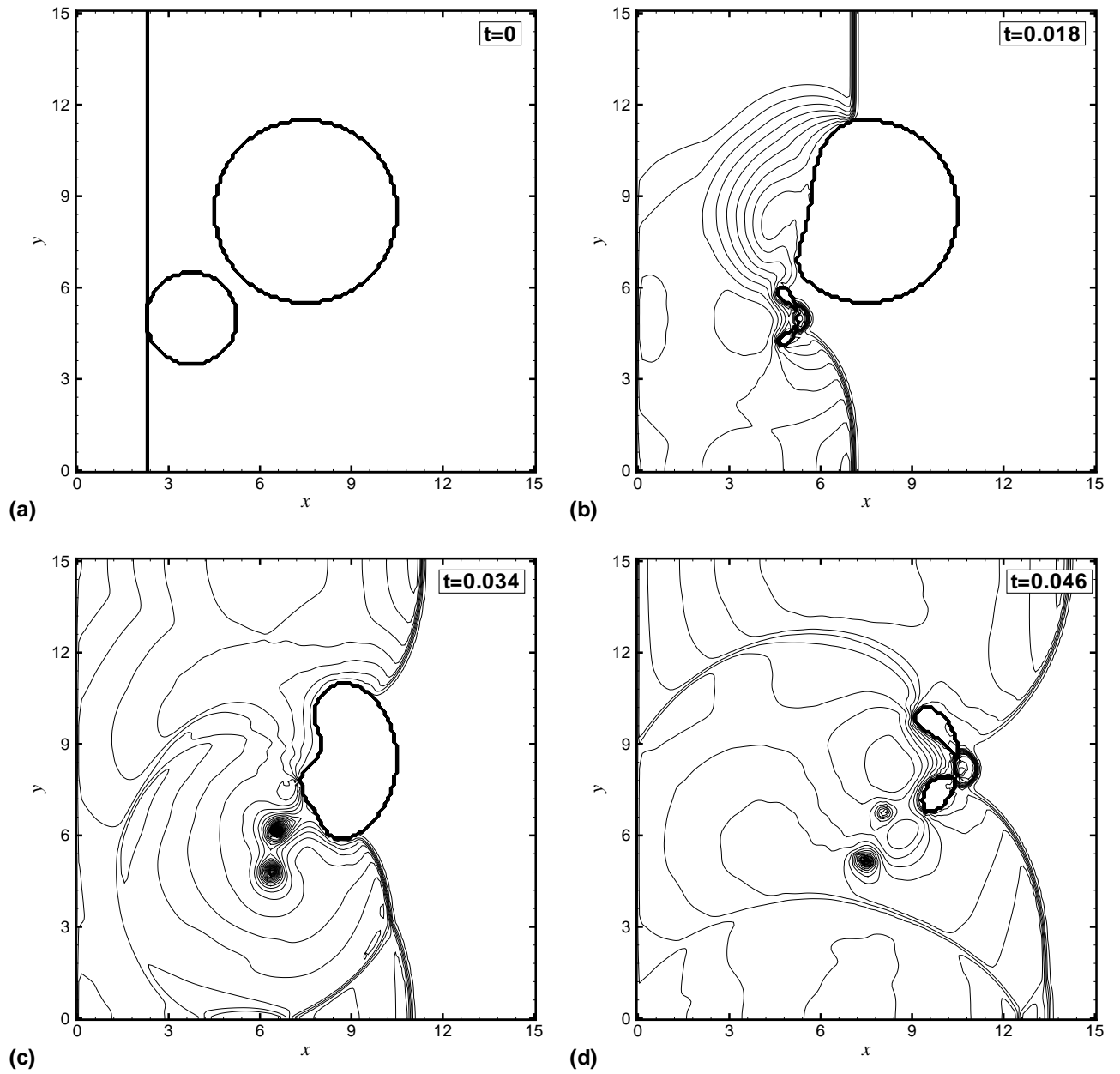Fig. 15. Case II-C: the pressure and density profiles for selected early time instances.

Fig. 16. Case II-D: 50 contours of density from 0 to 1.3 at different time instances
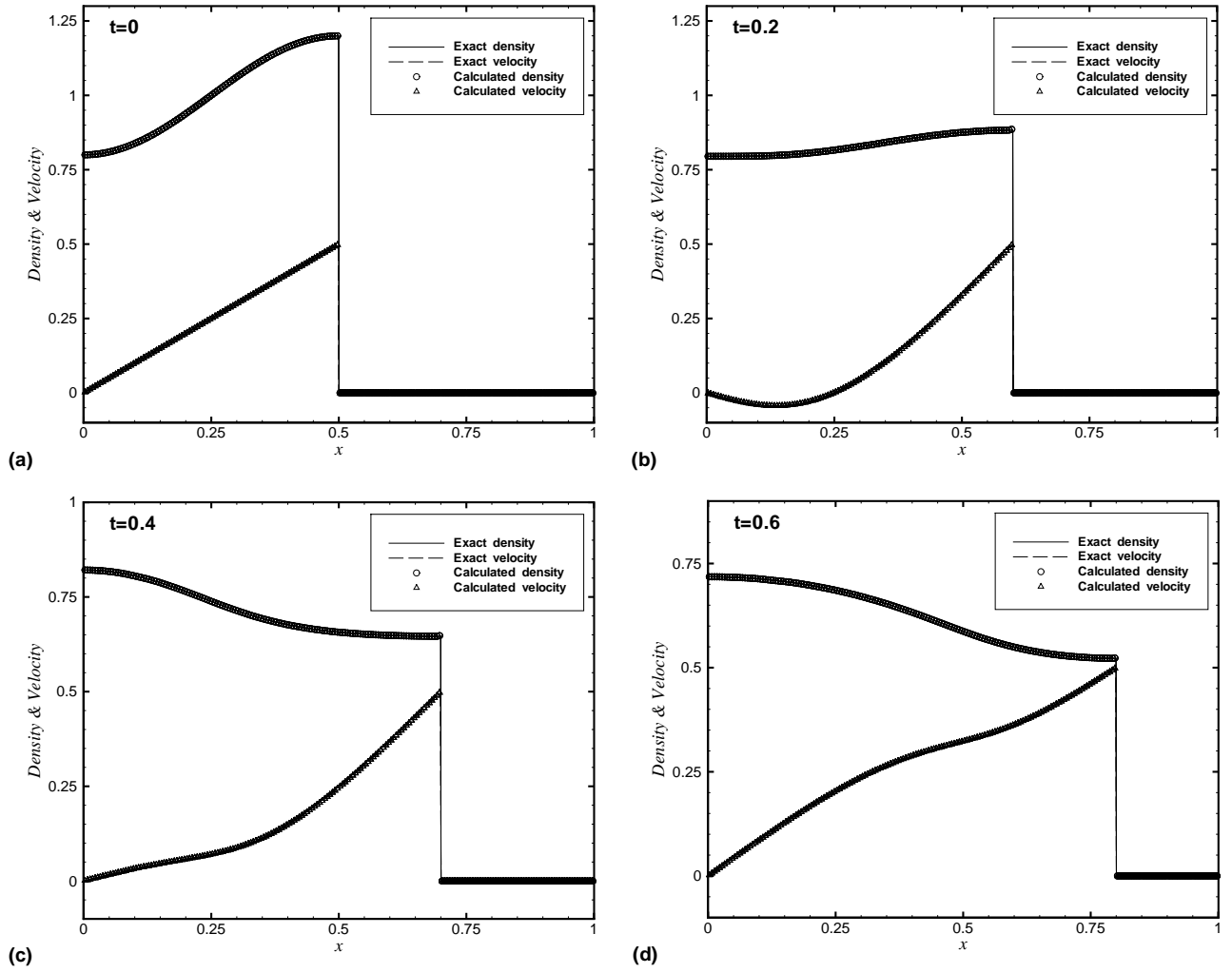
43

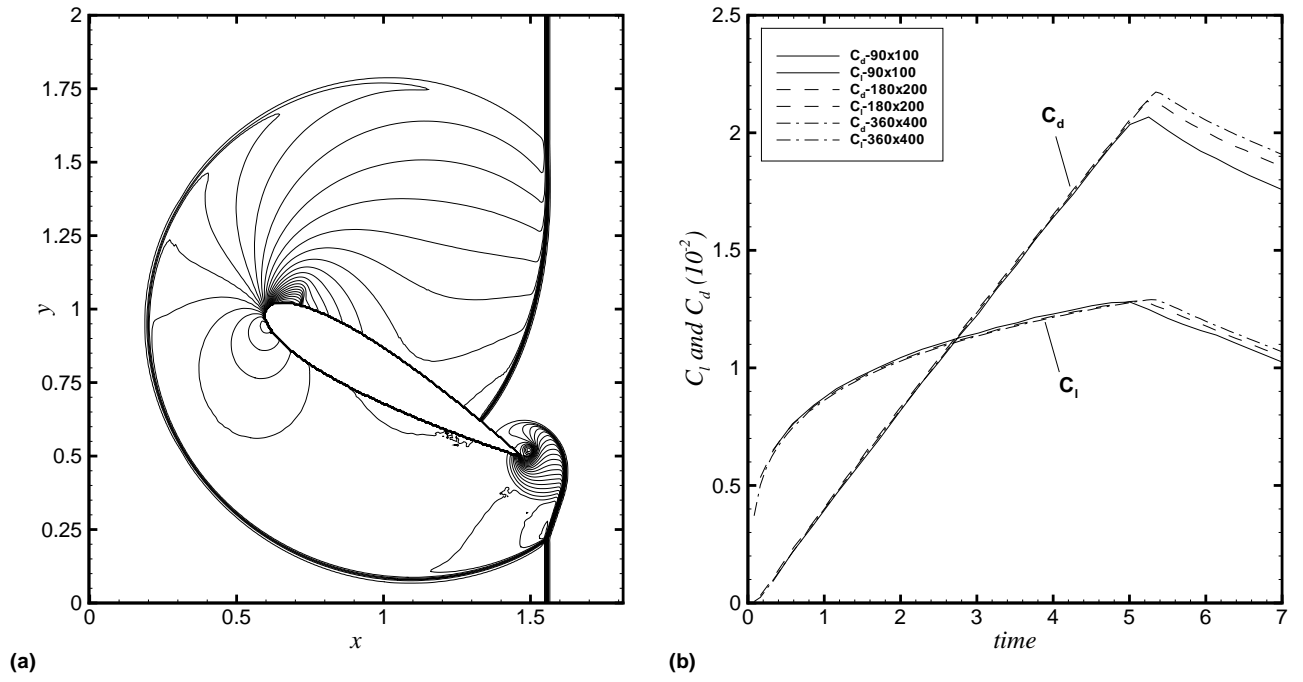Fig. 17. Case III-A: Moving wall problem.

44

Fig. 18. Case III-B: (a) 35 fluid pressure contours from 0 to 3.5, (b) time dependent lift and drag coefficients.
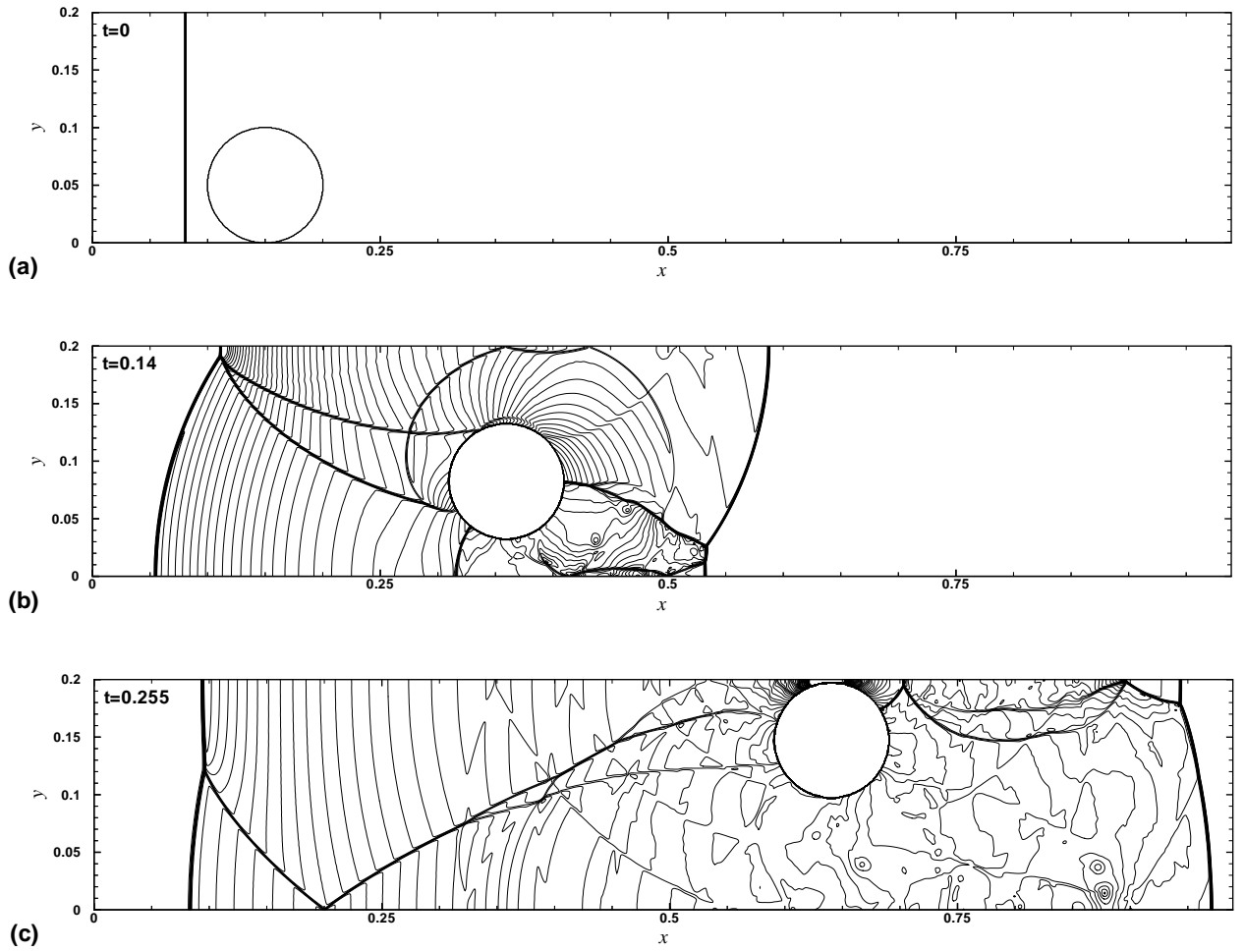
45

Fig. 19. Case III-A: 60 contours of fluid pressure from 0 to 28 for selected time instances.

List of Tables

Table 1
Errors and convergence rate for Case I-A.

$1/h$	$E_{s-}^{t=0.2}$	$E_{sT}^{t=0.2}$	$E_{s-}^{t=0.64}$	$E_{sT}^{t=0.64}$	$E_{s-}^{t=0.8}$	$E_{sT}^{t=0.8}$
50	3.7×10^{-4}	4.1×10^{-4}	5.2×10^{-3}	4.9×10^{-3}	6.7×10^{-3}	5.6×10^{-3}
100	2.6×10^{-5}	9.2×10^{-5}	2.1×10^{-3}	2.1×10^{-3}	3.1×10^{-3}	2.5×10^{-3}
200	4.9×10^{-6}	2.4×10^{-5}	7.1×10^{-4}	9.0×10^{-4}	1.1×10^{-3}	1.1×10^{-3}
400	4.0×10^{-7}	5.7×10^{-6}	1.2×10^{-4}	3.5×10^{-4}	2.8×10^{-4}	4.9×10^{-4}
R_c	3.3	2.5	1.8	1.3	1.6	1.2

Table 2
Errors and convergence rate for Case III-A.

$1/h$	50	100	200	400	800	R_c
err_{ttl}	2.9×10^{-4}	6.87×10^{-5}	1.71×10^{-5}	4.31×10^{-6}	1.07×10^{-6}	2.03
err_{bry}	4.06×10^{-3}	1.74×10^{-3}	7.7×10^{-4}	3.4×10^{-4}	1.5×10^{-4}	1.2